THESIS FOR THE DEGREE OF DOCTOR OF PHILOSOPHY

Terahertz sensing for pharmaceutical applications

Anis moradikouchi

Terahertz and Millimetre Wave Laboratory
Department of Microtechnology and Nanoscience-MC2
Chalmers University of Technology
Gothenburg, Sweden, 2023

Terahertz sensing for pharmaceutical applications

Anis moradikouchi

ORCID: 0000-0003-3811-1024

ISBN 978-91-7905-828-9
Doktorsavhandlingar vid Chalmers tekniska högskola, Ny series nr 5294
ISSN 0346-718X
This thesis has been prepared using LaTeX.

Chalmers University of Technology
Department of Microtechnology and Nanoscience-MC2
Terahertz and Millimetre Wave Laboratory
SE-412 96 Gothenburg, Sweden
Phone: +46 (0)31 772 1000
www.chalmers.se

Printed by Chalmers Reproservice
Gothenburg, Sweden, April 2023

To my beloved family.

Abstract

Pharmaceutical tablets are manufactured through the compaction of powder blends or granules in batch or continuous processes. In continuous manufacturing, real-time assurance of quality becomes essential to ensure that the final product meets the quality standards approved by manufacturers and regulatory authorities. Process analytical methods used for real-time monitoring and control should be rapid, non-destructive, and suitable to be conducted in the manufacturing area. This thesis demonstrates the terahertz frequency domain (THz-FD) technique, based on all-electronic solutions, as a fast, sensitive, and non-destructive sensing technique, with the advantage of a reasonable compromise between deep penetration depth and high spatial resolution, high dynamic range, and miniaturization capabilities. In this study, the THz-FD technique was explored to monitor the key physical properties such as tablet density and porosity through effective refractive index using a vector network analyser. In addition, taking advantage of the lower scattering effect of the THz region compared to higher frequencies, the feasibility of terahertz frequency domain spectroscopy (THz-FDS) combined with multivariate analysis to quantify drug content and tablet density was explored. As the quality of the tablets is highly impacted by the powder flow during manufacturing processes, it is beneficial to build quality assurance before the tableting process. In the last study, the capability of a terahertz frequency-modulated continuous wave (FMCW) radar was for the first time explored to characterise the powder flow dynamics in manufacturing processes. The velocity and density variations of falling powder streams in a vertical tube were non-invasively measured, using a 340-GHz radar instrument with a deep penetration depth through the powder flow and a sample volume resolution in the order of a few cubic centimeters.

In conclusion, it was demonstrated that the THz-FD technique and terahertz FMCW radar are highly promising as non-invasive process analytical tools for real-time quality monitoring of pharmaceutical powders and tablets.

Keywords: Pharmaceutical, powders, tablets, terahertz sensing, frequency domain spectroscopy, porosity, tablet density, multivariate analysis, API content, radar, powder flow characterization.

List of publications

This thesis is based on the following appended publications:

[A] **Anis Moradikouchi**, Martin Lindsjö, Jan Stake, Staffan Folestad, Helena Rodilla, “Non-Destructive Characterization of Pharmaceutical Tablets Using Terahertz Frequency Domain Spectroscopy,” in proceedings of the *44th International Conference on Infrared, Millimeter, and Terahertz Waves (IRMMW-THz)*, Paris, 2019, pp. 1–2, doi: 10.1109/IRMMW-THz.2019.8874004.

[B] **Anis Moradikouchi**, Anders Sparén, Staffan Folestad, Jan Stake, Helena Rodilla, "Terahertz Frequency Domain Sensing for Fast Porosity Measurement of Pharmaceutical Tablets," in *International journal of pharmaceutics*, 2022, doi: 10.1016/j.ijpharm.2022.121579.

[C] **Anis Moradikouchi**, Anders Sparén, Olof Svensson, Staffan Folestad, Jan Stake, Helena Rodilla, "Terahertz frequency-domain sensing combined with quantitative multivariate analysis for pharmaceutical tablet inspection," in *International journal of pharmaceutics*, 2022, doi: 10.1016/j.ijpharm.2022.122545.

[D] **Anis Moradikouchi**, Marlene Bonmann, Tomas Bryllert, Anders Sparén, Staffan Folestad, Jonas Johansson, Jan Stake, Helena Rodilla, "Terahertz radar diagnostics of powder dynamics in pharmaceutical manufacturing", manuscript under preparation, submitted to AstraZeneca PSO review, March 2023.

Acknowledgments

First and foremost, I would like to thank my main supervisor, Helena Rodilla, for the guidance, constant support, warm energy, encouragement, and fruitful discussions that I've had with her through the 5-year PhD journey. Secondly, I would like to thank my co-supervisor and examiner Jan Stake, for his support, encouragement, scientific discussions, and all I learned about writing and publishing. My big thanks to Anders Sparén, apart from being my great supervisor in the industry, I thank him for his support, encouragement, and discussions on multivariate analysis and experimental designs. Many thanks to Staffan Folestad for his supervision of my project, the fruitful discussions, and for showing me the bigger picture of the project. Also, thank you Olof Svensson and Mats Josefson for all the discussions on multivariate analysis. Thank you Jonas Johansson for supervising my project and giving feedback on the papers and thesis. Thank you Kristina Roos-Rydell, my manager at AstraZeneca, for all the help and support I received from you. Thank you Tomas Bryllert for all the discussions and feedback on radar systems. Thank you Mats Myremark for your help and creativity with the fabrication part of my measurement set-up in the shortest possible time.

A big thanks to my dear office mates, Juan and Marlene, whom I feel very lucky to have for their companionship, support, and warm vibes. I learned a lot from both of you in the scientific discussions. Juan, I appreciate our discussions about THz spectroscopy and material characterisation. Marlene, you taught me a lot about the radar system, and you were always there for me for the discussions and measurements; thank you very much. The same goes for the rest of my TML former and present colleagues (Divya, Junjie, Yin, Patrik, Xinxin, Mohammed Asad, Vladimir, Sergey, Peter, Andrei, etc).

A big thanks to my dear friends, whose presence and support warmed my heart through the PhD journey. I am grateful to Elham for her companionship and support through all the ups and downs during the last year. I would like to especially thank my boyfriend, Felix, for bringing so much love and happiness into my heart, and being the light of my life during all the good and challenging days. Lastly, I would like to give my sincere thanks to my beloved mother, father, brothers, Mojtaba, Mostafa, Morteza, and my sister, Najmeh, who always believed in me and supported me; I am who I am because of them.

This work was supported by the Swedish foundation for strategic research

(SSF), ID17-0011, and by AstraZeneca, PTD # 570, Gothenburg, Sweden.

Acronyms

API:	Active pharmaceutical ingredients
APICo:	API concentration
APIPS:	API particle size
BW:	Bandwidth
ComF:	Compaction force
DCP:	Calcium phosphate dibasic
FillPS:	Filler particle size
FMCW:	Frequency modulated continuous wave
MCC:	Microcrystalline cellulose
NIR:	Near-infrared
OPLS:	Orthogonal partial least squares
PLS:	Partial least squares
PMMA:	Poly-methyl methacrylate
PRI:	Pulse repetition interval
RMSEC:	Root-mean-square error of calibration
RMSECV:	Root-mean-square error of cross-validation
RMSEP:	Root-mean-square error of prediction
RPE:	Relative prediction error
SEM:	Scanning electron microscopy
SOLT:	Short, Open, Load, Through
TEM:	Transverse electromagnetic

THz-TDS:	Terahertz time-domain spectroscopy
THz-FD:	Terahertz frequency-domain
VNA:	Vector network analyzer

Mathematical symbols

c	Speed of light in vacuum
F	Compaction force
f	Frequency
f_d	Doppler shift
f_p	Porosity
f_{THz}	THz Porosity
G	Antenna gain
j	Imaginary unit, $\sqrt{-1}$
k_0	Wavenumber in vacuum
l	Sample thickness
$\hat{n}$	Complex refractive index
n_s	Real part of refractive index
P_r	Received signal power
P_t	Peak transmitted power
Q^2	Variances explained for cross-validation
R	Distance between radar antenna and moving object
R^2	variances explained for a calibration set
R_{max}	Maximum unambiguous range
S_{ij}	S-parameter from port j to port i
T	Complex transmission coefficient
V	Voltage
w	Concentration of the ingredients
Z	Characteristic impedance
Γ	Reflection coefficient
δ	Loss tangent
Δd	Cross-range resolution
ΔR	Range resolution
ΔV_s	Sample volume resolution
$\hat{\epsilon}$	Complex dielectric permittivity
ϵ'	Real part of dielectric permittivity
ϵ''	Imaginary part of dielectric permittivity
ϵ_{eff}	Effective permittivity

θ	Angle between beam and horizontal axis
κ_s	Imaginary part of refractive index
λ	Wavelength
λ_0	Wavelength in vacuum
ρ_{tablet}	Tablet density
ρ_{true}	True density
$\rho_{tab,THz}$	THz tablet density
σ_b	Back-scattering cross-section
τ	time delay
ϕ	Phase of transmission

Contents

CHAPTER 1

Introduction

1.1 Introduction

In the pharmaceutical industry, tablets are one of the most convenient dosage forms for the administration of drugs to patients. Tablets are bulk assemblies of solids in the form of powder particles, and gases in the form of air voids. A typical tablet formulation consists of active pharmaceutical ingredient(s) (API) and excipients with different functionalities, such as fillers, binders, and lubricants. Powders as raw materials are fed into the manufacturing process, undergo different interconnected manufacturing steps, and tablets are obtained as the final product. The quality of the tablets is highly sensitive to the initial characteristics of the powder particles entering the operation and their powder flow properties during processing [1]. Powder flow properties influence tablet properties, such as tablet density, porosity, mass, and drug content uniformity, which play a crucial role in the disintegration and dissolution of tablets [2]. The assessment of powder flow properties during manufacturing and the assessment of tablet properties as the final product is essential to ensure that the final product fulfills the required specifications. In this context, there is an increased need, especially in continuous manufac-

turing, to build quality control into the manufacturing process, using process analytical tools. These should be fast and non-destructive, enabling the implementation into the production line for real-time monitoring and control [3]. Various techniques for inspecting the properties of blends and tablets have been developed over the past years. Many of these techniques, such as mercury porosimetry and X-ray tomography, are typically slow, destructive, and not suitable for real-time sensing. Near-infrared spectroscopy [4]–[8] and Raman spectroscopy[9], [10] are common process analytical techniques to quantify drug content and assess the uniformity of drug content of powders and tablets. However, due to the short wavelength, these techniques suffer from scattering effects and limited penetration depth. Moreover, these techniques often require careful development and validation of robust multivariate calibration models. Electrical capacitance measurements enable the monitoring of powder flow properties based on variations in permittivity [11]. However, the requirement for a large number of capacitive probes for high spatial resolution limits its application. Acoustic emission and active sonic techniques have been used to characterize tablets and powder flow [12]. However, these techniques offer a low spatial resolution, the noise level is high, and the signal can get contaminated by other sources of sound waves[13].

Researchers have proposed terahertz radiation as an alternative technique to overcome the above-mentioned challenges [14], [15]. The terahertz frequency range lies between the microwave and infrared regions. Compared to the infrared region, terahertz waves are less vulnerable to scattering effects as a result of longer wavelengths. This feature provides a deeper penetration depth into powders and tablets, offering the characterization of a larger sample volume. The advantage of terahertz waves compared to microwave techniques is the higher spatial resolution, since the diffraction-limited resolution scales with the wavelength. Finally, the very low energy level of terahertz waves (4 meV at 1 THz) makes this technique non-ionizing and non-destructive.

Terahertz sensing as a fast non-destructive tool for pharmaceutical applications [15] allows the real-time monitoring of physical properties of powders and tablets. Terahertz time-domain spectroscopy (THz-TDS) was typically the selected technique for terahertz dielectric characterisation of tablets [16]. The correlation between the effective refractive index and tablet porosity was studied using a terahertz spectrometer[17]. Bawuah et al. used THz-TDS to obtain the porosity of tablets composed of one excipient [18] and later tablets

consisting of several excipients and an API [3]. Naftaly et al. proposed the use of THz-TDS to analyze the open porosity and scattering loss of powder compacts [19]. THz-TDS to assess tablet porosity and particle fragmentation during tableting has also been studied [20]. A lab-experimental THz-TDS set-up for monitoring powder flow densification was studied in [21]. THz-TDS instrumentation is a versatile tool for tablet characterisation in a lab environment. However, the miniaturisation of THz-TDS systems for implementation in production lines still remains a challenge.

In this thesis, the terahertz frequency domain technique (THz-FD), based on all-electronic solutions, is proposed as a fast, sensitive, and non-destructive sensing technique with high dynamic range and miniaturisation capabilities required for a future compact measurement system for in-line sensing [22]–[25].

In the first studies [Papers A and B], tablet density and porosity were assessed based on the effective refractive index of tablets at the terahertz frequency range. The effective refractive index of tablets was extracted from the transmission measurement of the scattering parameters of tablets using a vector network analyser and quasi-optical components across the frequency range of 325-500 GHz and 500-750 GHz. The mean value of the refractive index over the frequency range was used for extracting porosity. The results showed that the THz-FD measurements were highly sensitive to minute changes in tablet density and porosity, due to the change of materials and varying design factors, such as the particle size of the filler and the API, the compaction force, and the API concentration.

In the next study [Paper C], offering the advantage of the lower scattering effect, the feasibility of terahertz frequency domain spectroscopy (THz-FDS) combined with multivariate analysis to quantify API concentration and tablet density was explored. The terahertz signal was measured in transmission mode using the same set-up as in paper B, but across the frequency range of 750 GHz to 1.5 THz. This frequency range was chosen based on the presence of the absorption peaks of the ingredients of the tablets. Orthogonal partial least squares (OPLS) regression was applied to the spectral data to develop quantitative models for API concentration and tablet density. A fair model was obtained for API concentration and a high-quality model for tablet density.

In the last study [Paper D], a terahertz frequency-modulated continuous wave (FMCW) radar with a center frequency of 340-GHz [26] was for the

first time proposed to characterize the flow dynamics of powders in processing pipelines mimicking manufacturing operations. A set-up was designed for dispensing powder particles and flowing them through a vertical tube to simulate typical vessels in manufacturing processes. The radar successfully monitored real-time powder dynamics, such as powder flow velocity, density distribution and variations, and the position of powder streams inside the tube for different mass flow rates, particle sizes, and materials. Overall, the terahertz FMCW radar was demonstrated to be a promising diagnostic tool for remote sensing and process monitoring of the flow properties of powder streams in manufacturing processes.

CHAPTER 2

Interaction of terahertz waves with solids

This chapter describes the interaction of terahertz waves with solids. Section 2.1 presents the basics of terahertz spectroscopy for two main techniques, terahertz time-domain spectroscopy (THz-TDS), and terahertz frequency-domain spectroscopy (THz-FDS) which is the main focus of this thesis. In the THz-FDS technique, the scattering parameters explained in section 2.2) are used to study the propagation of electromagnetic waves in a medium, as explained in section 2.3. Section 2.4 explains the interaction of electromagnetic waves with a particle. Lastly, section 2.5 describes the interaction of electromagnetic waves with a moving object emitting from a radar system.

2.1 Terahertz spectroscopy for tablet characterisation

Terahertz spectroscopy has recently emerged as a fast non-destructive technique for real-time tablet characterisation that tackles the existing limitations of other vibrational spectroscopy techniques, such as scattering effects, short penetration depth, and complex nature of the measured spectra with the need

for multivariate calibration techniques. The terahertz spectral region is defined in the range of 100 GHz (3 mm) to 10 THz (30 μm), which is between the millimeter and the far-infrared region of the electromagnetic spectrum. The longer wavelength of terahertz waves compared to Near-infrared region provides deeper penetration depth and lower scattering effects. This permits to probe tablets and extract information that represents bulk properties of materials [27]. Additionally, the low photon energy of terahertz radiation makes it a safe sensing method.

2.1.1 terahertz time-domain spectroscopy

Terahertz time-domain spectroscopy (THz-TDS) has been the reference technique for terahertz spectroscopy, which has recently gained increasing interest in the pharmaceutical industry. THz-TDS is based on the interaction of short terahertz pulses with matter. This technique measures both the amplitude and phase information of the transmitted signal through a sample. An ultra-fast laser sends optical pulses with femtosecond pulse duration into a photoconductive antenna to be transformed into a picosecond terahertz pulse. Usually, the pulse is guided and focused on the sample via off-axis parabolic mirrors. The terahertz pulse interacts with the sample under test and is collected at the detector together with the beam from the delay line [27], [28].

This technique has the advantages of a wide frequency bandwidth from 100 GHz to 2 THz, with the downside of being a bulky measurement set-up that needs careful alignment of the optical components [3].

2.1.2 terahertz frequency-domain spectroscopy

terahertz frequency-domain spectroscopy (THz-FDS) is based on the interaction of pulse or continuous electromagnetic waves with matter. One approach for THz-FDS is electronic solutions based on heterodyne transmitters and receivers [29]. A vector network analyser is a key instrument in THz-FD technique for measuring the scattering parameters of materials, which will be explained in Sec. 2.2. In this method, a vector network analyser (VNA) along with two frequency extenders, two horn antennas, and off-axis parabolic mirrors or lenses (if needed, in order to focus the beam on the sample), see Fig. 2.1, are used to emit continuous electromagnetic waves to a sample and measure the scattering parameters of the sample, both phase and amplitude

of the reflection and transmission coefficients. The VNA generates sinusoidal continuous waves, which are up-converted to the terahertz range by the frequency extenders [29]. The first horn antenna, after the frequency extender, transmits the generated terahertz signal, which is then guided and focused on the sample by optical components. After probing the sample, the signal is guided by the optical components to the second horn antenna. The signal is down-converted to the low frequencies by the second frequency extender and is transferred to the VNA. The advantages of this technique are high-frequency resolution, high dynamic range [30], high SNR, and the possibility of set-up miniaturisation. The downside is that the measurement bandwidth is restricted to the bandwidth of rectangular waveguides before horn antennas. This method is currently available for frequencies up to 1.5 THz.

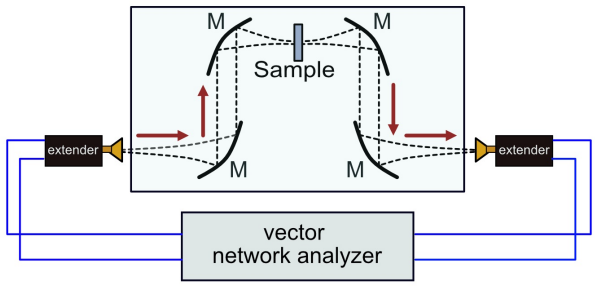

Figure 2.1: Schematic of a terahertz frequency-domain measurement set-up, consisting of a VNA, frequency extenders, and quasi-optical components.

2.2 Scattering parameters

Scattering parameters provide a complete description of a network, device, or material under test, relating the voltage wave incident to the system to those reflected and transmitted, as in:

$$S_{ij} = \left.\frac{V_i^-}{V_j^+}\right|_{V_{k\neq j}^+=0}, \tag{2.1}$$

where V_i^- is the voltage reflected from port i and V_j^+ is the voltage incident to the port j, while other ports are terminated with a matched load. As depicted in Fig. 2.2, for a two-port network we have:

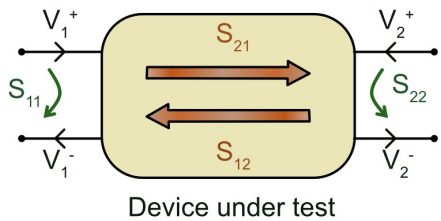

Figure 2.2: Illustration of the scattering parameters of a sample under test.

$$\begin{bmatrix} V_1^- \\ V_2^- \end{bmatrix} = \begin{bmatrix} S_{11} & S_{12} \\ S_{21} & S_{22} \end{bmatrix} \begin{bmatrix} V_1^+ \\ V_2^+ \end{bmatrix}, \tag{2.2}$$

In this thesis, considering the tablets under test symmetric and reciprocal, we have:

$$S_{11} = S_{22}, \tag{2.3}$$

$$S_{12} = S_{21}. \tag{2.4}$$

where S_{11} is the reflection coefficient at port 1, Γ, while port 2 is terminated with a matched load, S_{22} is the reflection coefficient at port 2 while port 1 is terminated with a matched load. S_{12} is the transmission coefficient, T, from port 2 to port 1 while port 1 is terminated with a matched load, and S_{21} is T from port 1 to port 2 while port 2 is terminated with a matched load [31], [32]. It should be mentioned that in the case of the cascade connection of two or more networks/materials, it is advantageous to transfer the scattering matrix to the transmission (ABCD) matrix [33].

2.3 Propagation of electromagnetic waves in a medium

The refractive index of a medium, $\hat{n}_s$, is a number that describes the behaviour of a propagating electromagnetic wave through this medium. It is the ratio

of the velocity of light in vacuum and in the medium. The refractive index is a complex number with real and imaginary parts, $\hat{n}_s = n_s - j\kappa_s$. The real part, n_s, indicates the phase velocity, while the imaginary part, κ_s, indicates the attenuation of the electromagnetic wave when it propagates through the medium.

On the other hand, the permittivity of a medium is a measure of the electric polarisability of the medium when subjected to an external electric field. The electric field causes the polarisation of the atoms or molecules of the material to create electric dipole moments. A material with high permittivity polarises more and creates a larger dipole moment in the direction of the electric field. The real part of permittivity describes the material's ability to interact with the electric field without absorbing energy, while the imaginary part shows the material's ability to permanently absorb energy.

The real and imaginary parts of the permittivity can be written in terms of the complex refractive index as in equation 2.5:

$$\begin{aligned} \hat{\epsilon}_r &= \epsilon_r' - j\epsilon_r'' = \hat{n}_s^2, \\ \epsilon_r' &= n_s^2 - \kappa_s^2, \\ \epsilon_r'' &= 2n_s\kappa_s. \end{aligned} \tag{2.5}$$

For a material with negligible conductivity, the ratio of the imaginary to the real part of the permittivity is called loss tangent, as in:

$$tan\ \delta = \frac{\epsilon''}{\epsilon'}. \tag{2.6}$$

TEM wave propagation in three-layer medium

The propagation of an electromagnetic wave through a three-layer medium can be modeled by using the theory of small reflections [31]. Let's assume a TEM plane wave traveling from medium 1 to medium 3 with a normal angle of incidence, see Fig. 2.3. Medium 1 and 3 are free space, and medium 2 is a dielectric with refractive index $\hat{n}_s$ and thickness l. The dielectric is homogeneous and has flat surfaces.

The total transmission from medium 1 to 3, T_t, can be obtained as an infinite sum of partial reflections and transmissions, as in:

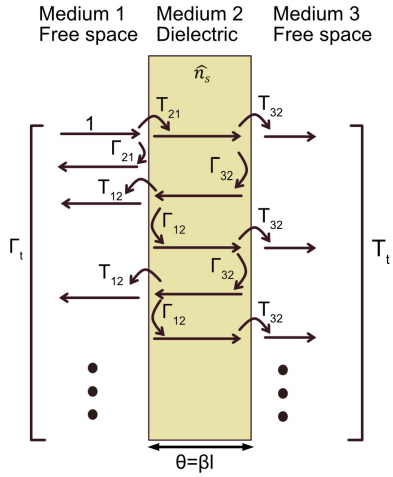

Figure 2.3: Partial reflections and transmissions on a three-layer medium.

$$T_t = T_{21}T_{32}e^{-j\theta} + T_{21}T_{32}\Gamma_{23}\Gamma_{21}e^{-j3\theta} + T_{21}T_{32}\Gamma_{23}^2\Gamma_{21}^2e^{-j5\theta} + ..., \tag{2.7}$$

where T_{mn} is the transmission coefficient from medium n to m, and Γ_{mn} is the reflection coefficient from medium n to m. The partial reflection and transmission coefficients can be computed as below:

$$\Gamma_{21} = -\Gamma_{12} = -\Gamma_{32} = \Gamma = \frac{Z_2 - Z_0}{Z_2 + Z_0} = \frac{\frac{Z_0}{\hat{n}_s} - Z_0}{\frac{Z_0}{\hat{n}_s} + Z_0} = \frac{1 - \hat{n}_s}{1 + \hat{n}_s}, \tag{2.8}$$

where Z_0 is the impedance of free space and Z_2 is the impedance of the dielectric.

$$T_{21} = 1 + \Gamma_{21},\ T_{32} = 1 + \Gamma_{32}, \tag{2.9}$$

Thus, T_t can be expressed as in:

$$\begin{aligned} T_t &= (1+\Gamma)(1-\Gamma)e^{-j\theta}(1+\Gamma^2 e^{-j2\theta}+\Gamma^4 e^{-j4\theta}+...)... \\ &= (1-\Gamma^2)e^{-j\theta}\sum_{i=0}^{\infty}(\Gamma^2 e^{-j2\theta})^i, \end{aligned} \tag{2.10}$$

Following the same procedure as for total transmission coefficient, the total reflection from medium 1 to 3, Γ_t, can be obtained as an infinite sum of partial reflections and transmissions [31], as in:

$$\begin{aligned} \Gamma_t &= \Gamma_{21}+\Gamma_{32}T_{21}T_{12}e^{-j2\theta}+\Gamma_{32}^2\Gamma_{12}T_{21}T_{12}e^{-j4\theta}+... \\ &= \Gamma\frac{1-e^{-j2\theta}}{1-\Gamma^2 e^{-j2\theta}}, \end{aligned} \tag{2.11}$$

and if the refractive index of the dielectric is close to 1, then $|\Gamma|^2$ is ≈ 0, so we can approximate:

$$T_t \approx e^{-j\theta}, \quad \Gamma_t \approx \Gamma(1-e^{-j2\theta}). \tag{2.12}$$

2.4 Interaction of electromagnetic waves with a particle

When electromagnetic waves illuminate a particle, the type of scattering depends on the ratio between the wavelength and the particle diameter. If the particle diameter is larger than around one-tenth of the incident wavelength, Mie scattering occurs. For particle sizes smaller than this ratio, the interaction of the wave with the particle is in the Rayleigh scattering range.

In Mie scattering, the interaction of the wave with the particle is such that the scattering in the forward direction is larger than in other directions, and the forward scattering intensity increases with the larger particles. The intensity of the Rayleigh scattering also increases with particle size, but is identical in forward and backward directions.

The radar used in this thesis measures the backscattered intensity. The backscattering cross-section for a single spherical particle is given by:

$$\sigma = \pi r^2 Q_b, \tag{2.13}$$

where r is the particle radius and Q_b is the backscattering efficiency, that can be obtained using Mie theory. Q_b depends on the particle's refractive index n and size, the wavenumber in the surrounding medium [34].

2.5 Radar technique for moving objects

Radar systems use electromagnetic waves to determine the distance (range) and velocity of moving objects relative to the radar. The transmitted electromagnetic waves (pulsed or continuous) reflect back from the objects to the radar, giving information about the location and velocity of the objects. Radar was first utilized for military use by several countries during World War II. The term RADAR as an acronym for radio detection and ranging [35]. Nowadays, radar systems are used in many different applications, including remote sensing of the environment, air-traffic control, radar astronomy, air-defense systems, marine radars, precipitation monitoring, flight control systems, and cars[36].

The back reflection signal off the targeted objects depends on the wavelength-to-particle size ratio and the target properties, such as the shape and the dielectric constant. Early radars used very long wavelengths compared to the size of the targets and detected very low signal intensity. The advance of high-frequency electronics pushed the operating frequencies of radars. Higher frequencies enable better range and cross-range resolution, and therefore, allow the detection of smaller particles. However, the output power limitation at high frequencies can restrict long-range applications [37].

Velocity measurement via the Doppler effect

Radar systems measure the velocity of an object via the Doppler effect. Doppler effect refers to the change in the electromagnetic wave frequency caused by the relative motion between a wave source and a reflecting object, such that if the object is moving either toward or away from the transmitter, there will be a slight change in the frequency of the reflected waves. The Doppler frequency shift measured by an active radar is related to the velocity of the moving object as follows:

$$f_d = 2f_t(\frac{v_r}{c}), \tag{2.14}$$

where f_d is Doppler frequency, f_t is transmitted frequency, v_r is the velocity of the object projected to the line of sight of radar, and c is the speed of light. When a reflecting object is moving at a 90-degree angle to the radar beam, it has no Doppler velocity. A target moving parallel to the radar beam gives the maximum Doppler frequency shift [36].

CHAPTER 3

Sample preparation

This chapter describes the tablet sets and the powders used in this work.

3.1 Tablet preparation

Different sets of tablets with two different formulations were used in the results presented in this thesis. The first formulation, explained in section 3.1.1, consisted of only excipients, and tablets were manufactured in a tablet press. These tablets were used to investigate the sensitivity of terahertz waves to tablets with different dielectric constants and compaction forces. The second formulation, explained in 3.1.2, consisted of API and excipients. These tablets were used to investigate the sensitivity of the terahertz waves to the variations of design factors such as the API concentration, the compaction force, and the particle size of powders.

3.1.1 First formulation

The tablet press Kilian S 300 (Romaco Kilian, Cologne, Germany) was used to manufacture the sets of tablets. Using a tablet press, it is possible to adjust

and control the mass and the compaction force applied to the powder compact in the tableting process, which results in tablets with different densities. This is achieved by making use of the adjustable lower and upper punches in the tablet press. The lower punch was used to adjust the mass of the tablets, and the higher punch was used to tune the compaction force applied to the tablets. This directly affects the height, density, and porosity of the tablets.

The tablets were flat faced and round with a diameter of 20 mm. The tablet height was measured several days after compaction to allow for mechanical relaxation. In each set, the mass of the tablets was kept constant, while different compaction forces were applied. As a result, tablets with different thicknesses and densities were produced. For a constant mass, thicker tablets have lower density and higher porosity.

Chemical components of tablets

Three tablet sets with different dielectric constants were produced. Set 1 was made of Microcrystallyne cellulose, set 2 of Succinic acid, and set 3 of Benzophenone. In each tablet set, there were seven tablets with different compaction forces.

A. Microcrystallyne cellulose (set 1)

Microcrystallyne cellulose (MCC) is a conventional pharmaceutical excipient used as a filler with advantages like tabletability, compatibility, and being suitable for direct compaction [38]. The characteristics of set 1 can be found in table 3.1. As can be seen, the height of the tablets decreases with increasing the compaction force. This causes the tablet density to increase and the tablet porosity to decrease.

B. Succinic acid (set 2)

Succinic acid is a common organic acid, which is used in different industries as a precursor to manufacture chemicals such as solvents, perfumes, lacquers, plasticizer, dyes, and photographic chemicals [39]. The characteristics of tablet set 2 can be found in table 3.2. The same trend explained in table 3.1 follows here.

Table 3.1: Data of tablet set 1, MCC.

Sample number	Height (mm)	Tablet density (gcm^{-1})	Compaction force (kN)
1	3.464	0.276	22.3
2	3.326	0.287	25.5
3	3.234	0.295	28.9
4	3.163	0.302	31.2
5	3.125	0.306	33.5
6	3.052	0.313	38.1
7	2.967	0.322	48.3

Table 3.2: Data of tablet set 2, Succinic acid.

Sample number	Height (mm)	Tablet density (gcm^{-1})	Compaction force (kN)
1	3.066	0.312	10.6
2	3.015	0.317	13.2
3	2.944	0.324	16.9
4	2.913	0.328	18.5
5	2.823	0.338	29.5
6	2.795	0.342	31.9
7	2.763	0.346	38.7

Table 3.3: Data of tablet set 3, Benzophenone.

Sample number	Height (mm)	Tablet density (gcm^{-1})	Compaction force (kN)
1	2.913	0.232	4.0
2	2.809	0.241	6.4
3	2.717	0.249	9.8
4	2.650	0.255	14.3
5	2.600	0.260	16.7
6	2.583	0.262	20.1
7	2.532	0.267	24.5

C. Benzophenone (set 3)

Benzophenone is used as a flavour ingredient, fragrance enhancer, and as an additive for plastics, coatings and adhesive formulations, and to prevent ultraviolet light-induced damage to cosmetics [40]. The characteristics of tablet set 3 can be found in table 3.3. The same trend explained in table 3.1 follows here.

3.1.2 Second formulation

A sample set of 69 tablets consisting of an API (ibuprofen), an excipient (mannitol), and a lubricant (magnesium stearate) was studied. Ibuprofen is a drug substance widely used for treating pain, fever, and inflammation [41]. Ibuprofen particles are needle-shaped with low flowability [42]. Mannitol is a widely used filler in the formulation of chewable or rapidly disintegrating tablet formulations. It is water soluble, nonhygroscopic, produces a semisweet taste, and has good compactibility [43]. Magnesium stearate is widely used as a lubricant for pharmaceutical tableting; it is relatively inexpensive, provides high lubrication with a high melting point and chemical stability [44]. A full factorial design of the API median particle size at two levels of ($d_{50} \sim 71$, 154 μm) and the excipient median particle size at two levels of ($d_{50} \sim 91$, 450 μm) were set, where the d_{50}-value is the median diameter of the particle size distribution found at 50% in the cumulative distribution. This design was repeated at five API concentration levels ($\sim$ 16, 18, 20, 22, and 24 w/w %), and Magnesium stearate concentration was kept $\sim$ 1 w/w% for all tablets. Details about the design of experiments can be found in table 3.4, where experiments 21–23 are center points that are used in the evaluation of the design to estimate the experimental precision. Tablets from all powder blends were manufactured at three compaction forces ($\sim$ 8, 12, and 16 kN), resulting in 69 different tablets. All tablets were flat faced, with a nominal weight of 300 mg, a diameter of 10.0 mm and a thickness in the range of 2.9–3.4 mm. Information about the tablets parameters are given in table 3.5.

Table 3.4: Design of experiments for the tablets from the second formulation. Design factors are API median particle size at two levels (71, 154 μm) , excipient median particle size at two levels (91, 450 μm), API concentration at five levels (16, 18, 20, 22, 25 w/w%) and compaction force at three levels (8, 12, 16 kN) (not included in the table).

Experiment number	API particle size d_{50} (μm)	filler particle size d_{50} (μm)	API concentration (w/w%)
1	71	91	16
2	154	91	16
3	71	450	16
4	154	450	16
5	71	91	18
6	154	91	18
7	71	450	18
8	154	450	18
9	71	91	20
10	154	91	20
11	71	450	20
12	154	450	20
13	71	91	22
14	154	91	22
15	71	450	22
16	154	450	22
17	71	91	24
18	154	91	24
19	71	450	24
20	154	450	24
21	95	211	20
22	95	211	20
23	95	211	20

3.2 Powder preparation

Three common pharmaceutical powders were used in the study for the characterisation of powder flows, which will be discussed later in chapter seven. The powders included microcrystalline cellulose (MCC), PEARLITOL 100 SD Mannitol, and calcium phosphate dibasic anhydrous (DCP). The particle size of the MCC powders was varied at three levels with d_{50} of 100 μm (MCC-100), 350 μm (MCC-350), and 500 μm (MCC-500), where, d_{50}, is the median diameter size of the particle size distribution. The particle size for Mannitol and DCP was 100 μm in both cases.

Table 3.5: List of characterised tablets for the second formulation. The ingredients were Ibuprofen, Mannitol Parteck M100 and Mannitol Parteck M200, Mannitol Pearlitol 400DC, magnesium stearate. The thickness of each tablet was measured five times by a micrometer. Tablet density was calculated from the weight and dimensions of tablets, and the true density of compact powder was calculated as will be explained in chapter four.

Tablet	Thickness (mm)	Mass (mg)	Tablet density (g cm^{-}3)	True density (g cm^{-}3)	API con. (w/w %)	Com. force (kN)
Set 1						
1	3.340	306	1.166	1.433	16.8	7.4
	3.190	306	1.221		16.8	12.2
	3.106	306	1.254		16.8	16.0
2	3.325	304	1.164	1.436	16.2	7.9
	3.175	304	1.219		16.2	12.1
	3.089	304	1.253		16.2	15.9
3	3.072	303	1.256	1.432	16.0	8.0
	2.976	303	1.296		16.0	11.8
	2.926	303	1.318		16.0	15.8
4	3.095	305	1.255	1.431	16.2	8.4
	3.015	305	1.288		16.2	11.9
	2.956	305	1.314		16.2	15.9
Set 2						
5	3.298	303	1.170	1.425	18.5	8.2
	3.174	303	1.216		18.5	12.2
	3.076	303	1.254		18.5	15.8
6	3.356	306	1.161	1.427	18.0	7.9
	3.203	306	1.216		18.0	12.0
	3.121	306	1.248		18.0	15.9
7	3.123	306	1.248	1.421	18.4	8.2
	3.029	306	1.286		18.4	12.1
	2.961	306	1.316		18.4	15.8
8	3.117	307	1.254	1.424	17.9	8.5
	3.057	307	1.278		17.9	11.9
	3.014	307	1.297		17.9	15.3
Set 3						
9	3.321	304	1.165	1.416	20.6	8.2
	3.180	304	1.217		20.6	12.2
	3.103	304	1.247		20.6	16.0
10	3.371	307	1.160	1.419	19.9	7.8
	3.250	307	1.203		19.9	11.7
	3.146	307	1.242		19.9	15.4
11	3.066	302	1.254	1.417	19.5	8.0
	2.985	302	1.288		19.5	11.9
	2.972	302	1.294		19.5	15.2
12	3.144	306	1.239	1.418	19.3	8.4
	3.054	306	1.276		19.3	12.0
	3.008	306	1.295		19.3	16.0

Tablet	Thickness (mm)	Mass (mg)	Tablet density (g cm^{-}3)	True density (g cm^{-}3)	API con. (w/w %)	Com. force (kN)
Set 4						
13	3.335	304	1.161	1.407	22.7	8.3
	3.195	304	1.212		22.7	11.9
	3.133	304	1.236		22.7	16.1
14	3.336	304	1.160	1.409	22.2	8.3
	3.230	304	1.198		22.2	11.8
	3.129	304	1.237		22.2	15.6
15	3.124	303	1.235	1.402	22.9	7.9
	3.012	303	1.281		22.9	13.0
	2.973	303	1.298		22.9	16.0
16	3.154	305	1.231	1.408	21.4	7.9
	3.071	305	1.264		21.4	11.7
	3.041	305	1.277		21.4	14.6
Set 5						
17	3.348	304	1.156	1.398	24.8	7.8
	3.215	304	1.204		24.8	11.8
	3.151	304	1.228		24.8	15.5
18	3.375	307	1.158	1.401	24.1	8.0
	3.270	307	1.195		24.1	11.5
	3.154	307	1.239		24.1	15.8
19	3.142	304	1.232	1.393	25.0	7.8
	3.050	304	1.296		25.0	12.1
	3.021	304	1.281		25.0	15.6
20	3.148	305	1.234	1.398	23.8	8.5
	3.064	305	1.267		23.8	12.3
	3.036	305	1.279		23.8	16.0
21	3.372	309	1.167	1.419	20.0	8.7
	3.240	309	1.214		20.0	12.3
	3.164	309	1.244		20.0	16.1
22	3.378	307	1.157	1.418	20.1	8.3
	3.241	307	1.206		20.1	11.8
	3.107	307	1.258		20.1	16.7
23	3.378	305	1.149	1.417	20.4	7.9
	3.204	305	1.212		20.4	12.0
	3.097	305	1.254		20.4	15.9

CHAPTER 4

Terahertz characterisation of pharmaceutical solids

This chapter describes the terahertz frequency-domain measurements set-up used for the characterization of tablets in section 4.1, the extraction method of effective refractive index from scattering parameter measurements and its translation to tablet porosity in section 4.2, multivariate analysis in section 4.3, and finally the terahertz radar set-up used for powder flow characterisation in section 4.4.

4.1 Measurement set-up for tablet characterisation

Free space frequency-domain measurements in transmission mode was used to characterise the tablets under study through scattering parameters measurements. Free space measurement is contact-less, non-destructive and doesn't require sample preparation. The first set-up consisted of a VNA (Keysight PNA-X), frequency extenders, and diagonal horn antennas (VDI), see Fig. 4.1. The Gaussian beam after the horn antenna expands as it is traveling in the free space, and due to the large diameter of the beam reaching the tablet, this

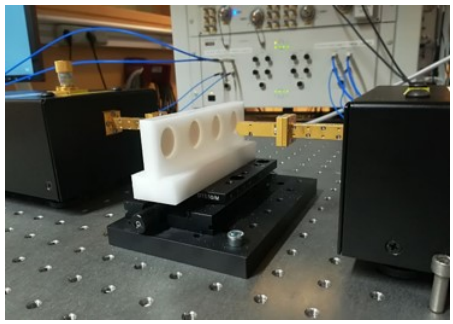

Figure 4.1: Photograph of experimental set-up in transmission mode for scattering parameters measurements.

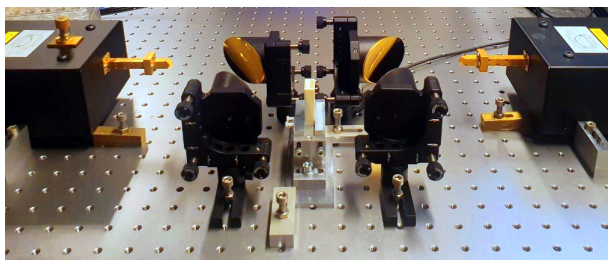

(a)

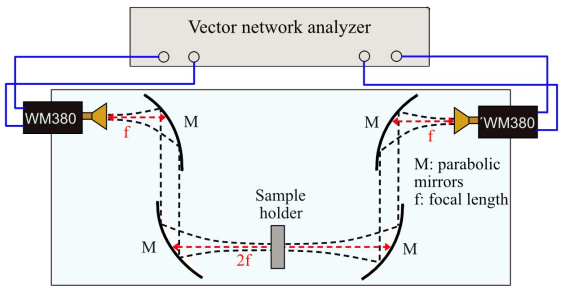

(b)

Figure 4.2: a) Photograph and b) schematics of the experimental set-up showing terahertz scattering parameter measurements in transmission mode. The blue square represents the area showed in the photograph.

set-up is restricted to tablets with a large diameter. This set-up was used in [Paper A] for the tablets with the first formulation with a diameter of 20 mm. The frequency range was 325-500 GHz, provided by VDI frequency extenders 570 WM. It is possible to manipulate the beam and have a smaller beam diameter by adding four parabolic mirrors to collimate and focus the beam on the samples, see Fig. 4.2. This facilitates the measurements of tablets with smaller diameters, with the cost of being bulkier. This set-up was used for the tablets with the second formulation with a diameter of 10 mm. The frequency range selected was 500-750 GHz, 750 GHz-1.1 THz, and 1.1-1.5 THz, using VDI frequency extenders WM-380, WM-250, and WM-164, respectively [Papers B and C]. In all measurements, the empty holder was used as the reference for relative measurements. Relative measurements suppress the uncertainty due to possible misalignment of components, loss in the optical path, and temperature and humidity variation.

4.2 Effective refractive index and porosity extraction

The complex effective refractive index of the tablets can be extracted from relative measurements of the complex transmission coefficients ($T = S_{21}$) between the sample and air. In this thesis, two different methods were used for the extraction of the effective refractive index. The first method, multiple reflections, considers the small reflections of terahertz waves inside the tablet. The second method, one-path transmission, simplifies the extraction of $\hat{n}_s$ by ignoring the small reflections, and is suitable for low-loss mediums.

The effective refractive index is assumed to be homogeneous across the tablets, and the electromagnetic wave at the surface of the tablets is assumed to be a plane wave with a normal angle of incidence. In this work, the focus was on the real part of the refractive index for characterising the tablet density and porosity. The imaginary part can be used for other purposes, like studying the moisture content.

4.2.1 Multiple reflections

In this method, $\hat{n}_s$ can be extracted from the comparison of the measured relative transmission coefficients with a modeled one [45]. The relative trans-

mission between sample and air, T_s/T_a, can be modeled as in equation 4.1 [46]:

$$\left(\frac{T_s}{T_a}\right)_m = \frac{(1-\Gamma_1^2)}{1-\Gamma_1^2 e^{-2jk_0\hat{n}_s l}} e^{-jk_0 l(\hat{n}_s-1)}, \tag{4.1}$$

where the total transmission, T_t in Fig. 4.3, has been used to consider the

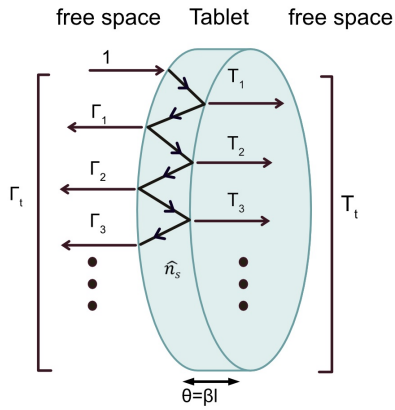

Figure 4.3: Partial transmissions and reflections inside a tablet.

multiple reflections inside the tablet. k_0 is the free space wave number, and l is the thickness of the tablet. Γ_1 is the complex reflection coefficient in the interface between air and tablet, as in:

$$\Gamma_1 = \frac{1-\hat{n}_s}{1+\hat{n}_s}. \tag{4.2}$$

The value of $\hat{n}_s$ versus frequency was obtained numerically by solving equation 4.3:

$$f(\hat{n}_s) = \left(\frac{T_s}{T_a}\right)_m - \left(\frac{T_s}{T_a}\right)_d = 0. \tag{4.3}$$

where $(T_s/T_a)_d$ is the measured relative transmission data. This equation has multiple possible solutions because of the periodic nature of the exponential terms. To find the correct solution, $n_{s,i}$ from the equation below was used as an initial estimate:

$$n_{s,i} = 1 + \frac{\tau c}{2\pi l}, \tag{4.4}$$

where c is the speed of light in vacuum and τ is the time delay, $\tau = -\frac{\Delta\phi}{\Delta\omega}$, which is the slope of the phase of measured relative transmission versus frequency [47], [48]. In order to verify the results, the model, $(T_s/T_a)_m$, was recalculated using the obtained $\hat{n}_s$, and its magnitude and phase were compared with the measurement data, $(T_s/T_a)_d$ [Paper B].

4.2.2 One-path transmission

In this method, the multiple reflections of waves inside the tablets are neglected. The imaginary part, κ_s, can be extracted from the amplitude of the relative transmission, which will not be discussed here. The real part of $\hat{n}_s$, n_s, can be obtained from the phase shift of the relative transmission, using only the first transmission path, T_1, in the Fig. 4.3, as in [49]:

$$n_s = 1 - \frac{(\Delta\phi - 2m\pi)\lambda}{2\pi l}, \tag{4.5}$$

where $\Delta\phi = \phi - \phi_0$ is the relative phase shift of the transmission coefficient between sample and empty holder, l is the tablet thickness, and m is the number of wavelength inside tablets. m accounts for the possible phase ambiguity, which can be caused due to the multiple wavelengths inside thick tablets (compared to the wavelength of terahertz waves). The phase ambiguity can be addressed by approximating the number of the wavelength, as in:

$$(n_{s,0} - 1)\frac{l}{\lambda_0} - \frac{1}{2} < m < (n_{s,0} - 1)\frac{l}{\lambda_0} + \frac{1}{2}, \tag{4.6}$$

where λ_0 is the wavelength in free space, $n_{s,0}$ is the initial guess for n_s.

This method is simple, but neglects the multiple reflections inside the tablets and requires an initial guess for n_s to calculate m [Paper A].

As it was mentioned, a plane wave has been assumed for this extraction, whereas the nature of the propagating beam from horn antennas is Gaussian beam. Modeling the relative transmission considering Gaussian beam propagation would give higher accuracy for n_s [48]. However, as the horn antennas used in this thesis were diagonal horns with a maximum Gausisity of 86%, the Gaussian beam propagation model was not included.

4.2.3 Porosity extraction

Porosity, f_p, can be calculated using equation 4.7 [50]:

$$f_p = 1 - \frac{\rho_{tablet}}{\rho_{true}}, \tag{4.7}$$

where ρ_{tablet} is the density of the tablet and ρ_{true} is the true density of the powder blend.

Porosity can be obtained manually through tablet density, by measuring the weight and volume of the tablet, but this would be time-consuming and not suitable for real-time measurements. In order to address this, tablet density can be obtained from the effective refractive index of tablets measured by the THz-FD technique. Given that the tablet density varies in a small range, a linear relation between the effective refractive index of tablets and tablet density can be assumed [51]. Therefore, tablet density can be obtained from the effective refractive index extracted from scattering parameter measurements, and it can be translated to porosity using equations 4.8 - 4.9:

$$\rho_{tab,THz} = \rho_1 n_s + \rho_0, \tag{4.8}$$

$$f_{THz} = 1 - \frac{\rho_{tab,THz}}{\rho_{true}}, \tag{4.9}$$

where $\rho_{tab,THz}$ and f_{THz} are the tablet density and porosity obtained from terahertz measurements, respectively. In order to obtain the coefficients, ρ_1 and ρ_0, the tablet density obtained from mechanically measurement of mass and volume of the samples can be used for calibration.

ρ_{true} in equation 4.7 can be calculated from the concentration, w_i, and the true density of the constituents, $\rho_{true,i}$, from literature and their data sheet, as in [50] [Paper B]:

$$\frac{1}{\rho_{true}} = \sum_{i=1}^{3} \frac{w_i}{\rho_{true,i}}. \tag{4.10}$$

4.3 Multivariate analysis

A multivariate calibration is a quantitative mathematical model in which many variables are used simultaneously to predict one or more parameters,

according to a predefined mathematical equation with given coefficient values. In this thesis, the measurement of the absorbance spectrum of tablets to obtain information on the drug content via the application of mathematical methods such as partial least square error is an example of multivariate calibration. The type of data in this thesis is first-order measurements, meaning per sample or observation, the measurement data is represented as a vector with many variables (multivariate response), for instance, the absorbance spectrum. Some advantages of multivariate analysis are noise reduction, selectivity, increased sensitivity, and outlier detection [52].

4.3.1 Partial Least Squares regression

Partial Least Squares regression (PLS) aims to model the relationship between two sets of variables, typically a set of predictor variables (X) and a set of response variables (Y). A PLS model reduces the dimensionality of X space into a smaller set of uncorrelated variables and finds the direction in the X space that explains the maximum variance in the Y space. In other words, in PLS Regression, the relationship between the predictor variables and the response variables is modeled through components or latent variables. The components are derived by finding linear combinations of the predictor variables that explain the maximum covariance with the response variables. The first component explains the maximum covariance and subsequent components explain remained unexplained covariance.

4.3.2 Orthogonal Partial Least Squares

OPLS is a modification of the partial least squares (PLS) regression. OPLS separates the variability in the X data into two parts, one that is predictive of the Y response and another that is orthogonal to Y. In the case of just a single Y variable and with the condition of the same number of components, both PLS and OPLS models fitted to the same data will give identical predictions. By separating the predictive and non-predictive variation in the predictor variables, OPLS improves the interpretability of the results. Multivariate analysis is an important tool for qualitative and quantitative analysis of multivariate spectral data.

Orthogonal partial least squares (OPLS) regression [53] was used to establish a prediction model for the quantification of API concentration and

tablet density. The tablets were divided into two sets: calibration set and test set. The calibration set was used to build a model for the response, called the calibration model. In the calibration set, the variances explained for the calibration set (R^2) and the cross-validation (Q^2), the root-mean-square of the calibration (RMSEC), and the root-mean-square of the cross-validation (RMSECV) were used to assess the model performance. Cross-validation is a model validation method that uses different portions of the calibration set iteratively to train and test the model.

The test set was applied to the calibration model to challenge the robustness of the model for the prediction of unknown samples. The root-mean-square error of prediction (RMSEP) was used to evaluate how well the test samples fit the calibration model. Relative prediction error (RPE) is the RMSEP normalized with the mean value of the response, measuring the accuracy of the prediction regardless of the nature of the response [Paper C].

4.4 Radar for powder flow characterisation

In this study, a terahertz frequency-modulated continuous-wave (FMCW) radar was used for the characterisation of powder flow in a vertically positioned tube. The FMCW radar, radar measurements, and powder flow in a tube will be discussed below.

4.4.1 FMCW radar

FMCW is capable of measuring the distance between the radar antenna and an object in addition to the velocity of the moving object; therefore, it provides the possibility to measure the powder particle distribution along the radar beam. Sawtooth wave modulation is widely used in FMCW radars to change the frequency pattern of the emitted radio wave. The physical distance from the radar to the reflecting object, R, for a FMCW radar with Sawtooth wave modulation, can be obtained through the equation below [37]:

$$R = \frac{c\Delta fT}{2BW}, \tag{4.11}$$

where BW is the frequency sweep bandwidth, T is the frequency sweep time, and Δf is the frequency shift between the transmitted and reflected signal

due to the range, assumed to be constant, see Fig. 4.4. Please note that Δf is due to the travel time of the signal for the specific range, and f_d is due to the velocity of the object. For a slow-moving object and a radar with a short sweep time T_p, $f_d < \Delta f$.

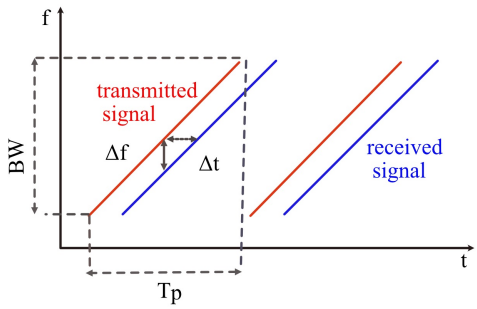

Figure 4.4: Sawtooth modulation in FMCW radar system

The equation below expresses the received signal power, P_r, which is reflected from an individual scatterer, based on Frris transmission formula: [36]:

$$P_r = \frac{P_t G^2 \lambda^2 \sigma_b}{(4\pi)^3 R^4}, \tag{4.12}$$

where P_t is the peak transmitted power, G is the antenna gain, λ is the wavelength of the signal, and σ_b is the back-scattering cross-section of the scatterer.

The radar beam range resolution, ΔR, is defined by:

$$\Delta R \approx \frac{c}{2BW}, \tag{4.13}$$

where BW is the pulse bandwidth. The cross-range of the beam is defined by the radar beamwidth. The radar beam cross-range resolution, Δd, is defined by:

$$\Delta d \approx \frac{cR}{f_c D}, \tag{4.14}$$

where f_c is the center frequency, and D is the diameter of the radar antenna.

Therefore, the sample volume resolution is then defined by:

$$\Delta V_s = \pi \Delta R (\Delta d/2)^2 \tag{4.15}$$

4.4.2 Radar measurement setup

A monostatic 340-GHz FMCW pulse-Doppler radar developed at the Chalmers University of Technology [54], was used for the powder flow characterization, see Fig. 4.5. Linearly frequency-modulated pulses with 30-GHz bandwidth and about milli-Watt output power are transmitted to the powder stream. The received signal of 128 pulses, within a coherent time of 6.6 ms, is computed to obtain the velocity profile and the position of the powder stream relative to the radiating horn antenna. The powder velocity component along the radar beam direction is determined by the measured Doppler shift. A radar image frame interval of 346 ms was used. The instantaneous bandwidth of 30 GHz provides a radar range resolution of 5 mm. The radar's optical system provides an almost collimated beam with a radius w of about 1 cm at 150 cm away from the radar.

The powder flow dynamics were studied in three different configurations: i) the radar beam incident from the bottom of the tube parallel to the stream as in Fig. 4.6a, ii) the radar instrument positioned on the side and at the upper part of the tube with an incident angle $\theta \sim 5$ deg as in Fig. 4.6b; and iii) the radar on the side and at the lower part of the tube with an incident angle $\theta \sim 5$ deg, as in Fig. 4.6c. θ is the angle formed between the beam and the x coordinate. The angle θ of the incident beam is needed for the radar side measurements to detect a powder velocity component non-orthogonal to the radar line of sight. In addition, the θ angle lowers the strong back reflections from the tube walls.

The radar was located about 154 cm away from the tube for the configurations shown in Figs. 4.6 a and b, and about 107 cm away for the configuration Fig. 4.6c.

4.4.3 Powder flow in a tube

An experimental set-up was designed to mimic the powder flow in common pharmaceutical equipment. First, the powder particles were dispensed in a discharge hopper with a conical bottom with evenly distributed holes. This

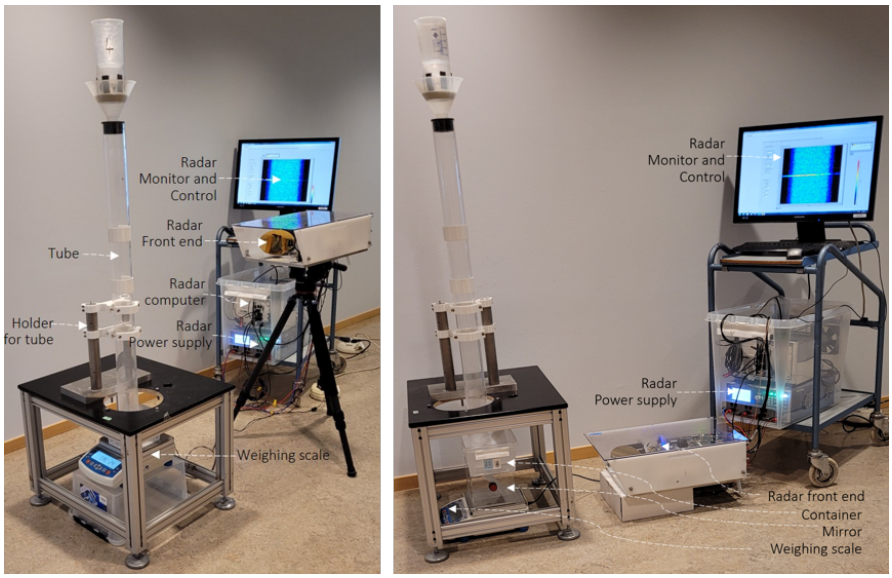

Figure 4.5: Radar measurement set-up for the characterisation of powder flow

hopper provides a constant height of materials above the holes. The size and number of the holes define the powder mass flow rate. Too small holes cause the formation of solid bridges over the holes and, therefore, blockage or low mass flow rate, whereas larger holes provide a higher mass flow rate. The discharge hopper is located on a cylindrical tube with air gaps to allow the air intake from the surroundings for the particles in order to avoid the pulsing effect in the powder stream. The powder strings from the hopper holes enter a funnel and form a single powder stream at the lower opening of the funnel. The cross-section of the powder stream is determined by the size of the funnel's lower opening. The tube is made of poly-methyl methacrylate (PMMA) with a height of 100 cm, an outer diameter of 7 cm, and a 3-mm wall thickness. Finally, the powder particles land in a container located on a weighing scale, which continuously weighs the cumulative powder weight. The time derivation of the cumulative powder weight gives the powder mass flow rate. See Fig. 4.5, showing the experimental setup including feed hopper, funnel, tube, weighing scale, radar instrument, and computer.

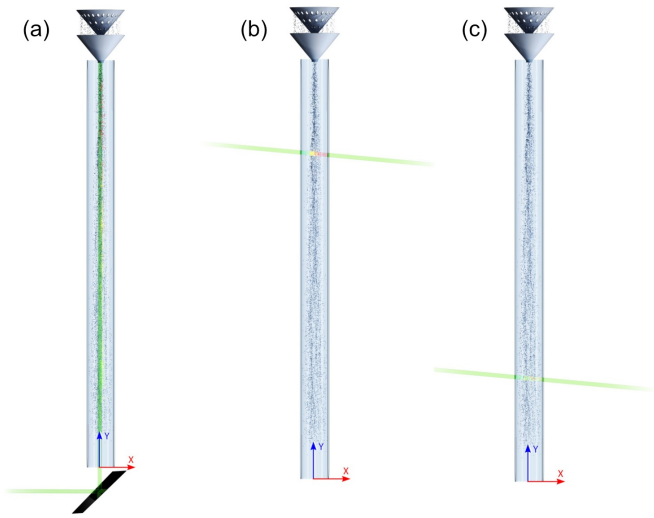

Figure 4.6: Illustration of the three radar positions used in this work. (a) Radar beam incident from the bottom of the tube, vertically, along the stream. (b) Radar beam incident from the side of the tube at the upper part of the tube, $y = 84$ cm, with an incident angle of $\theta = 5°$, and (c) radar beam incident from the side of the tube at the lower part of the tube, $y = 23$ cm, with an incident beam angle of $\theta \sim 5°$.

CHAPTER 5

Tablet density and porosity characterisation using THz-FD technique

This chapter shows the applicability of the THz-FD technique to characterise and quantify changes in tablet density/porosity. Section 5.1 presents the results for the effective refractive index extracted from THz-FD measurements and its correlation with the tablet density for tablets made of one ingredient and different compaction forces (first formulation in chapter three). Section 5.2 presents the results of the extracted effective refractive index for tablets containing API and excipient with varying design factors like API concentration or particle size (second formulation in chapter three). Finally, the translation of the effective refractive index to tablet porosity will be discussed.

5.1 Tablet density characterisation in single ingredient tablets

The effective refractive index of the tablets with the first formulation in chapter three was extracted, using the one-path transmission method presented in chapter four. Each tablet was measured four times to verify the repeatability

of the measurements. Before tablet measurement, the empty sample holder was measured as a reference for relative measurements. The phase shift of S_{21} across frequency was used to obtain the real part of the effective refractive index of the tablets.

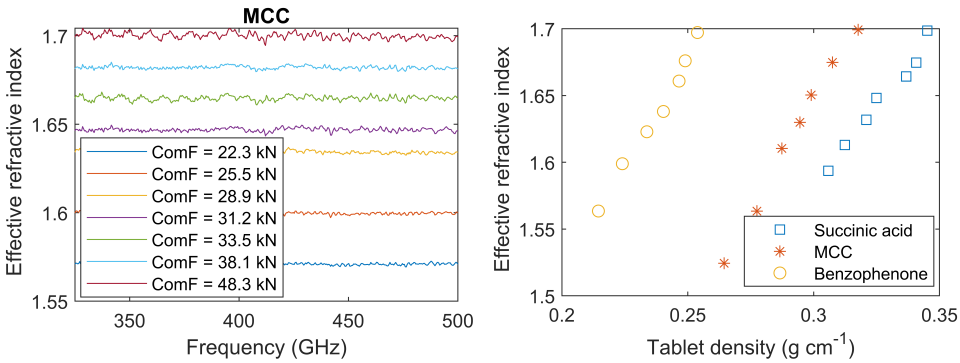

Figure 5.1: a) Effective refractive index versus frequency for MCC tablets with different compaction forces. Higher compaction force increases the effective permittivity. b) Effective refractive index versus tablet density, for benzophenone, MCC, and succinic acid tablets. For a specific effective refractive index, the benzophenone tablets show the lowest tablet density, followed by MCC and succinic acid tablets, respectively.

Fig. 5.1a shows the real part of the extracted effective refractive index versus frequency for MCC tablets with different compaction forces. As can be observed, increasing the compaction force resulted in a higher effective refractive index, as air voids in between particles were removed, which led to higher tablet density. This result verifies the sensitivity of terahertz waves to detect the change of the effective refractive index as a consequence of different compaction forces. Fig. 5.1b shows the effective refractive index versus manually measured tablet density, for each set of tablets at a fixed frequency point, 420 GHz. For a specific tablet density, the benzophenone tablets showed the highest effective refractive index, followed by MCC and succinic acid tablets, respectively. Moreover, a linear correlation between effective refractive index and tablet density was observed.

5.2 Tablet porosity characterisation

5.2.1 Effective refractive index extraction

Here, the effective refractive index of the tablets was studied by THz-FD technique at a frequency range of 500-750 GHz. Tablets were made of an API (ibuprofen), an excipient (mannitol), and a lubricant (magnesium stearate) with a full factorial design of the API and excipient particle size, API concentration, and compaction force. The frequency range was chosen to avoid the absorption peaks of Ibuprofen and Mannitol. Each frequency sweep took less than one second to complete, having an intermediate frequency bandwidth of 1 kHz and a total number of frequencies of 251. Each tablet was measured ten times in consecutive frequency sweeps to verify the measurement repeatability. The real part of the effective refractive index, n_s, was obtained from the phase of the measured relative transmission coefficients to study the properties of the tablets, using the multi-reflection method presented in chapter four. Fig. 5.2.a shows the comparison of the phase of the measured relative transmission with that of the model for three tablets with the same API and filler particle size, and API concentration, but three different compaction forces, F_1= 8 kN, F_2= 12 kN, F_3= 16 kN. The good agreement between the measurements and the model validates the extraction method.

Fig. 5.2b shows the extracted effective refractive index of the three tablets across frequency. As observed earlier in the tablets with a single ingredient, a higher compaction force increased the effective refractive index, because of the reduced air voids in between tablet particles. The minor oscillations observed in n_s are due to the standing waves within the measurement set-up and the fact that the tablet thickness used for the extraction is the measured one, not an effective tablet length, which in practice can be different due to the non-ideal beam properties and/or thickness and density inhomogeneities across the tablets. Fig. 5.3 shows the computed tomography scan of the tablet with experiment number 3 in table four chapter three. It can be seen that tablet density is higher at the center of the tablet, and the thickness is not homogenous at the top and bottom surface, which will affect the effective electrical path. It was observed in Fig. 5.2b that n_s is frequency independent. Hence, the mean value of the effective refractive index across the frequency band was chosen for data analysis.

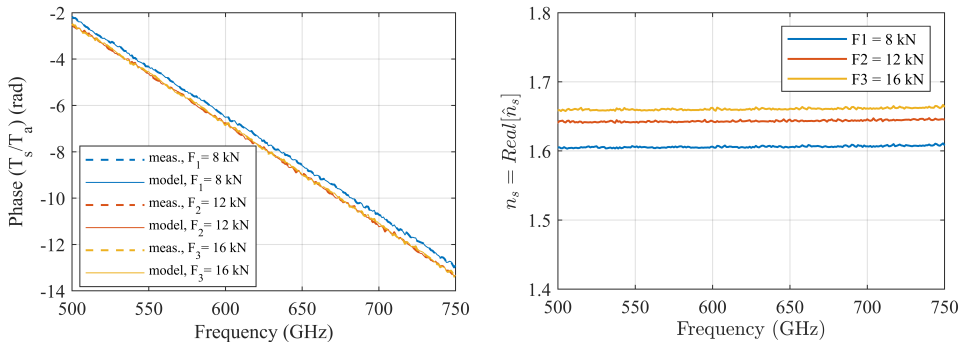

Figure 5.2: a) Phase of relative transmission for tablets (experiment number 2 in table four chapter three with three different compaction forces, F_1= 8 kN, F_2= 12 kN, F_3= 16 kN, showing good agreement between model and measurement data b) Real part of effective refractive index over frequency. A higher compaction force increased the effective refractive index.

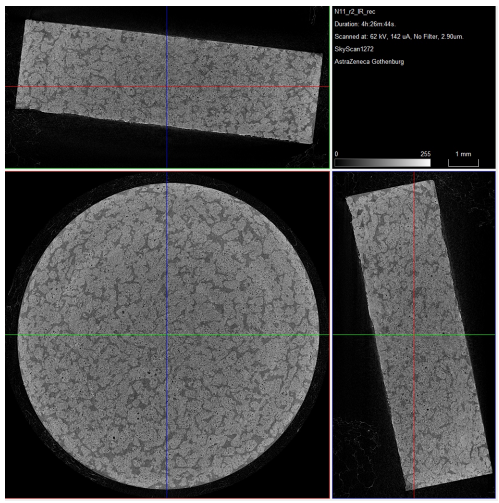

Figure 5.3: Computed tomography scan of a tablet with experiment number 3 in table four chapter three, showing the thickness/density inhomogeneities across the tablet.

5.2.2 Effective refractive index versus design factors

In this section, the sensitivity of the THz-FD measurements to the variation of the design factors, API and filler median particle size, API concentration, and compaction force is examined.

A multi-linear regression model was applied with the effective refractive index as the response and the design factors as the independent variables, describing the contribution of each design factor [55]. The statistical tool used for this purpose was MODDE 12 [56], and the obtained model is given as in equation 5.1:

$$n_s = \beta_0 + \beta_1 x_1 + \beta_2 x_2 + \beta_3 x_3 + \beta_{33} x_3^2 + \hat{e}, \tag{5.1}$$

where x_1 is the compaction force, x_2 is the API concentration, x_3 is the filler particle size, and $\hat{e}$ is the error in the model. β_0 is the average value of n_s, and $\beta_i, i = 1, 2, 3$ are the coefficients, showing the impact of each design factor on the response.

Fig. 5.4a shows the centered and scaled coefficients of the design factors, which are normalised and scaled to have a mean of zero. Error bars show the uncertainty in Δn_s from each design factor. It was observed that the filler particle size, FilPS, had a larger impact than API particle size, APIPS, due to having filler as the dominant portion of the tablets. Besides that, the compaction force, ComF, had a larger effect than the API concentration, APICo, because the interval chosen for the compaction force is larger in size compared to that of the API concentration. Figs. 5.4 (b-d) show the variation of n_s with respect to each design factor, using the multi-linear regression model presented in equation 5.1. It was observed that higher compaction force resulted in higher effective refractive index due to removing the air voids between particles (Fig. 5.4b), and increasing API concentration lowers the effective refractive index due to the fact that the refractive index of Ibuprofen is lower than Mannitol (Fig. 5.4c). It was also observed that larger particles were more prone to fragmentation and consolidation of the fragmented particles [57], leading to increased effective refractive index (Fig. 5.4d). Scanning electron microscopy (SEM) (Zeiss Supra 55) photographs of the cross-section of one tablet (experiment number 3 in table four chapter three) were taken to investigate the fragmentation of the particles. As can be seen in Fig. 5.5, the results showed a particle size reduction down to around 10 μm, which verified

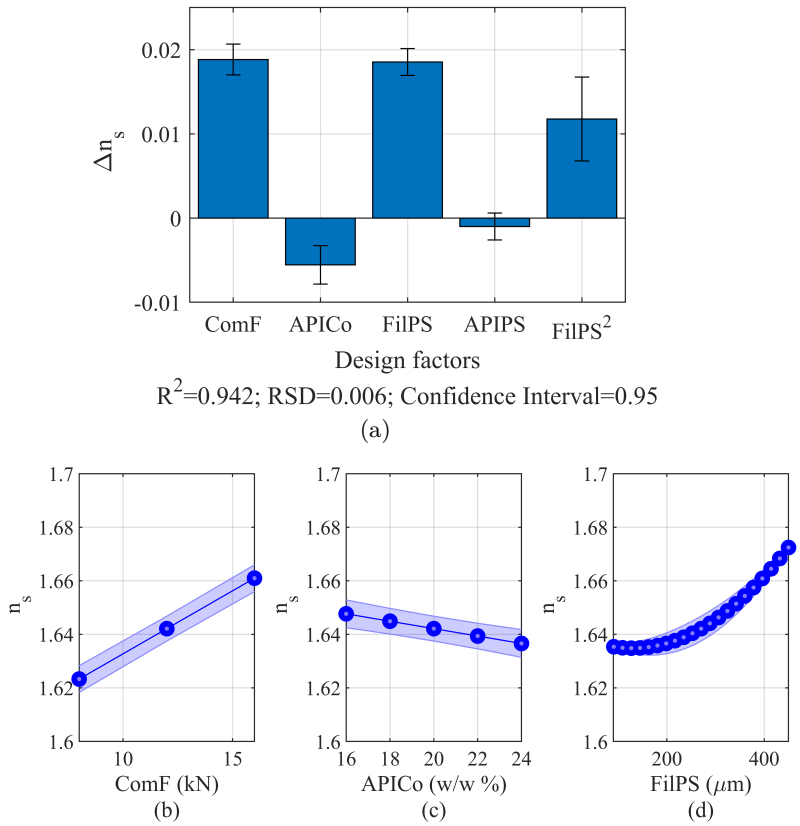

Figure 5.4: a) The change in n_s with respect to the design factors, when a factor varies from its average to high value, having the other factors at their averages. Compaction force is shown as ComF, filler particle size as FilPS, API particle size as APIPS, and API concentration as APICo. b-d) The variation of n_s with respect to the design factors. Plots are created using the multi-linear regression model in equation 5.1. In each plot, the line shows n_s and the shadowed area shows the standard deviation.

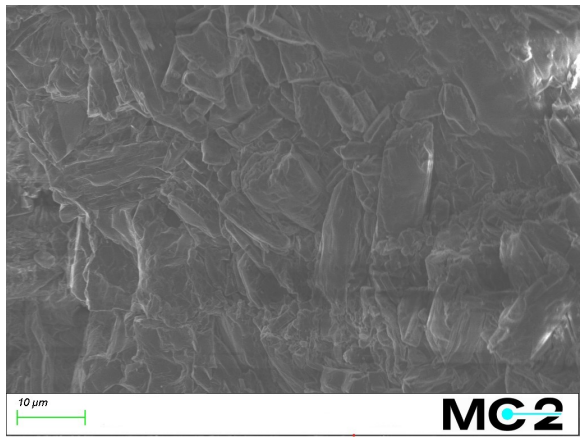

Figure 5.5: Scanning electron microscopy of a cross-section of a tablet (experiment number 3 in table four chapter three, with the initial particle size of 450 μm for excipient and 71 μm for API, respectively). The fragmentation of particles while tableting process is clearly seen in this picture.

the fragmentation deformation behavior of Mannitol and Ibuprofen, with the initial particle size of 450 μm and 71 μm respectively.

5.2.3 THz porosity versus design factors

In this section, the tablet porosity is extracted from the obtained effective refractive index from terahertz measurements. For this, a linear approximation between tablet refractive index and density was assumed and empirically verified. Later, the quantified THz porosity and its variation with respect to the design factors are shown.

Fig. 5.6a shows the linear correlation between the effective refractive index obtained from the measurements and tablet density estimated from mass and volume measurements, validating the assumed linear approximation. Fig. 5.6b shows the relationship between THz porosity and the effective refractive index of the tablets. The refractive index of the solid phase of the tablets for each API concentration, corresponding to zero porosity, can be estimated from the intercept with THz porosity equaling zero.

After the extraction of the tablet porosity, the effect of the design factors on the porosity was studied using the multi-linear regression method

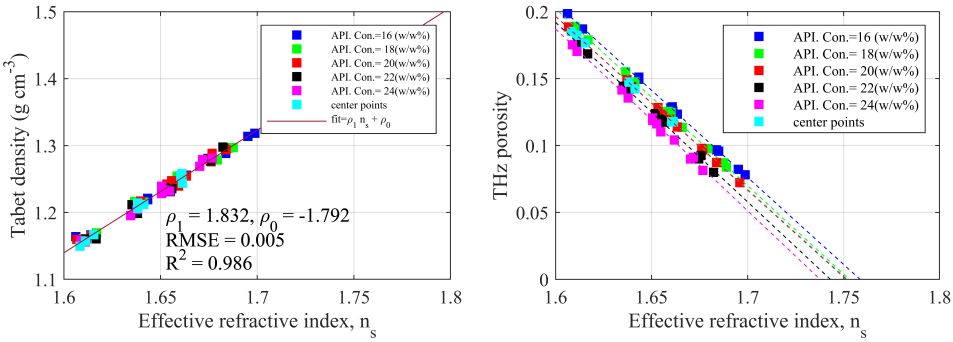

Figure 5.6: a) Correlation between the effective refractive index and tablet density. A linear relationship between the effective refractive index, n_s, and tablet density was observed. b) correlation between THz porosity and effective refractive index.

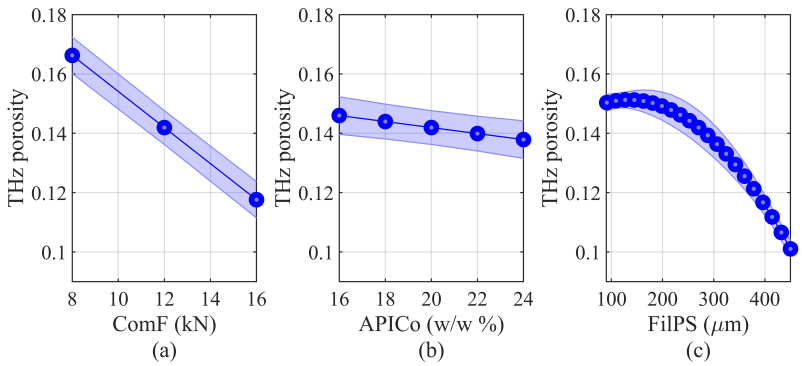

Figure 5.7: The variation of the THz porosity with respect to the design factors, a) compaction force, b) API concentration, and c) filler particle size. The plots were created using a multi-linear regression model similar to the equation 5.1. In each plot, the line shows the THz porosity and the shadowed area shows the standard deviation.

explained in section 5.2.2, being the extracted porosity the response of the system. Fig. 5.7a shows that increasing the compaction force lowers porosity, which is in agreement with the fact that a higher compaction force reduces the air voids in between particles and results in lower porosity. Fig. 5.7b shows the reduction of porosity with increasing the API concentration, showing the sensitivity of the THz-FD technique to the small variation of the API concentration from 16% to 24% [58]. The effect of filler particle size on porosity is shown in Fig. 5.7c. It is observed that increasing the particle size of the filler first results in a slight increase in the porosity for filler particle size smaller than 150 μm and then a decrease in the porosity for larger particles. This behaviour can be explained by fragmentation behaviour of Mannitol [59] and Ibuprofen [60] under compaction force during the tableting process, and the fact that there is a greater tendency for the larger particles to fragment under high compression pressure [57]. After the fragmentation, the particles consolidate and pack together, which results in lower porosity.

CHAPTER 6

Tablet API concentration and density characterisation using THz-FDS multivariate technique

This chapter shows the applicability of THz-FD spectroscopy in combination with multivariate analysis to quantify API concentration and tablet density. Section 6.1 presents the tablets' spectral data obtained from scattering parameters. In Section 6.2, the multivariate analysis results for quantifying API content are shown, and in Section 6.3, the multivariate analysis results for quantifying tablet density are presented.

6.1 Terahertz spectral data

The terahertz attenuation spectra of the tablets were used to characterise the absorption peaks of API and excipient, and develop prediction models for API content and tablet density based on spectral information. A fraction of a full factorial design from the second formulation presented in chapter three was used for this study. The design factors were Mannitol particle size varying at two levels ($d_{50} \sim 91$, 450 μm), API concentration varying at five levels ($\sim$ 16, 18, 20, 22, and 24 w/w %), and a fixed applied compaction force of 12 kN. As

shown in table 6.1, our sample set included 11 tablet types (A, B, ..., M), and for each tablet type, there were three replicate samples (A-1, A-2, A-3, B-1, ...) to account for the variations in each tablet type, resulting in 33 samples.

To obtain the attenuation spectra of the tablets, the complex transmission coefficients were measured in the frequency range from 750 GHz to 1.5 THz, including the absorption peaks of Mannitol and Ibuprofen. During measurements, the intermediate frequency bandwidth was set to 10 Hz in order to minimize the measurement noise level. Each frequency sweep took around one minute. Each sample was measured twice by dismounting and mounting the tablets in the sample holder to account for the measurement errors. This led to 66 measurements. The samples were labeled such that the first letter shows tablet type, the second part shows the number of the replicate sample, and the third part shows the number of measurements for each sample [paper C].

The attenuation coefficient of the samples, $\alpha(f)$, can be calculated from the measurement of the scattering parameters using equation 6.1 [62]:

$$\alpha(f) = -\frac{1}{l} log \left| \frac{T_s}{T_a} \right|^2 , \tag{6.1}$$

where l is sample thickness in cm, and T_s and T_a are the measured complex transmission coefficients (S_{21}) of the sample and empty sample holder (air), respectively. Fig. 6.1 shows the attenuation spectra of all measured tablets. The two peaks seen at around 1.1 THz and 1.5 THz are the superposition of the Ibuprofen and Mannitol peaks that heavily overlap. The peak occurring at around 1.1 THz was not completely resolved due to the low signal level consequence of the overlap of material absorption peaks with water absorption lines, together with a decreased signal-to-noise ratio(SNR) at the beginning of the frequency band of the extenders. As can be observed, noise, high-frequency oscillations from standing waves in the set-up, and a slanted baseline as a result of scattering effects and frequency-dependent absorption, were present in the measured terahertz spectra. In the next step, the measured samples were divided into two sets, including a training set and a test set. From the three replicates of each tablet type, the first two samples were used in the training set, and the third sample was used in the test set.

Table 6.1: Design of experiments for the tablets, a fraction of a full factorial design from reference [61]. Design factors are filler particle size at two levels (91, 450 μm) and API concentration at five levels (16, 18, 20, 22, 25 w/w%). There are three replicates for each tablet type.

Tablet	API median particle size d_{50} (μm)	Filler particle size d_{50} (μm)	API concentration (w/w%)	Tablet density (g cm^{-3})
Type A				
A-1	71	91	16.8	0.3061
A-2	71	91	16.8	0.3059
A-3	71	91	16.8	0.3058
Type B				
B-1	71	450	16.0	0.3248
B-2	71	450	16.0	0.3248
B-3	71	450	16.0	0.3246
Type C				
C-1	71	91	18.5	0.3033
C-2	71	91	18.5	0.3031
C-3	71	91	18.5	0.3042
Type D				
D-1	71	450	18.4	0.3206
D-2	71	450	18.4	0.3198
D-3	71	450	18.4	0.3220
Type E				
E-1	71	91	20.6	0.3043
E-2	71	91	20.6	0.3043
E-3	71	91	20.6	0.3042
Type F				
F-1	71	450	19.5	0.3219
F-2	71	450	19.5	0.3209
F-3	71	450	19.5	0.3210
Type G				
G-1	71	91	22.7	0.3014
G-2	71	91	22.7	0.3014
G-3	71	91	22.7	0.3021
Type H				
H-1	71	450	22.9	0.3200
H-2	71	450	22.9	0.3207
H-3	71	450	22.9	0.3191
Type K				
K-1	71	91	24.8	0.3025
K-2	71	91	24.8	0.3014
K-3	71	91	24.8	0.3023
Type L				
L-1	71	450	25.0	0.3180
L-2	71	450	25.0	0.3167
L-3	71	450	25.0	0.3186
Type M				
M-1	95	211	20.1	0.3010
M-2	95	211	20.1	0.3009
M-3	95	211	20.1	0.3003

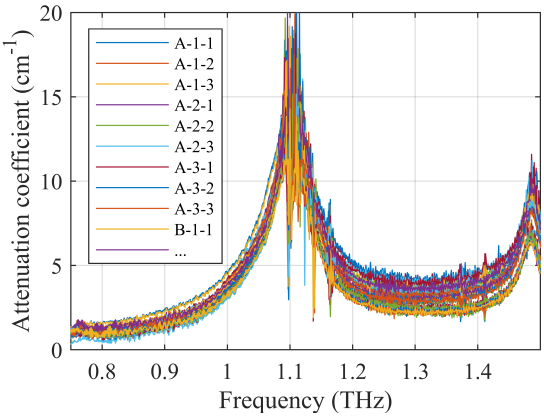

Figure 6.1: Spectral data for all samples from table 6.1.

6.2 OPLS model for API concentration

As the first step to model the API concentration, data treatment was performed on the raw data. A Savitzky-Golay smoothing filter [63] was used to reduce the effect of noise and oscillations. Then, asymmetric least squares algorithm [64] was used for each spectrum to correct baseline variations. Lastly, each spectral value was normalized with respect to the sum of the signal intensity over the frequency range. The data pre-processing was performed in SIMCA 17 (Sartorius Stedim Data Analytics, Umeå, Sweden), which is a software for multivariate data analysis.

In the next step, OPLS regression was applied to the scaled and centered treated training data set to establish a prediction model for API concentration. In OPLS regression, the frequency points were the independent X variables, and API concentration was the Y response. The parts of the spectrum including the absorption peaks have the dominant role in modeling the API response.

The first evaluation of the score plot revealed that tablet sets B and H were outliers, due to the day-to-day humidity variations, as they were measured on a different day with a high humidity level. After excluding the outliers and re-applying the OPLS regression, a good API concentration model with R^2 of 0.98 and Q^2 values of 0.92 was obtained.

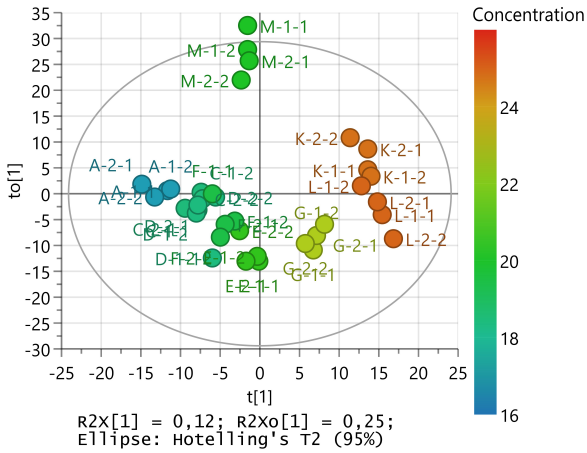

Figure 6.2: Score plot for API concentration. Tablets are clustered with respect to the API concentration across the horizontal axes. Tablets are labeled with three digits that represent type, replicate, and measurement number, respectively.

The score plot in Fig. 6.2 shows the clusters of the samples based on their similarity for modeling the API concentration. The variations across the horizontal axes show the predictive component of the response. The vertical direction expresses within clusters variability, which is unrelated/non-predictive to the response. In this plot, the horizontal direction corresponds to the five clusters of API level. Tablets are ordered from left to right by increasing API concentration. Moreover, the variations between replicate samples and the good repeatability of the measurements can be observed in this plot, following the second and third digits in the sample labels, respectively, based on the closeness of the observations.

Fig. 6.3a shows the observed versus predicted values for API concentration based on the OPLS regression. The R^2 was 0.98, and the RMSEC and RMSECV were 0.40 and 0.77, respectively. To challenge the robustness of the OPLS model, a test set was applied to the model. Fig. 6.3b shows the comparison between the reference and prediction results for the test samples. Five clusters corresponding to the API concentration level are observed, with about 3% error for sample G3. The RMSEP value was 1.22 and the relative

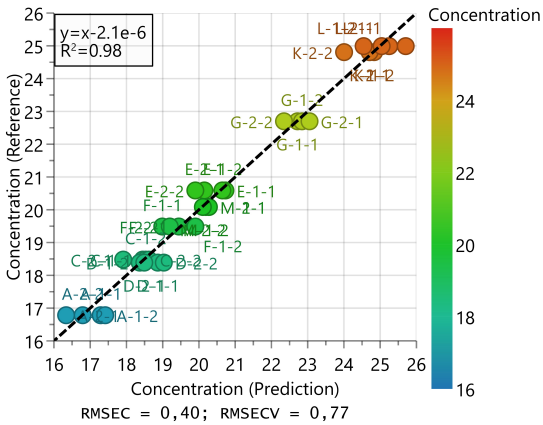

(a)

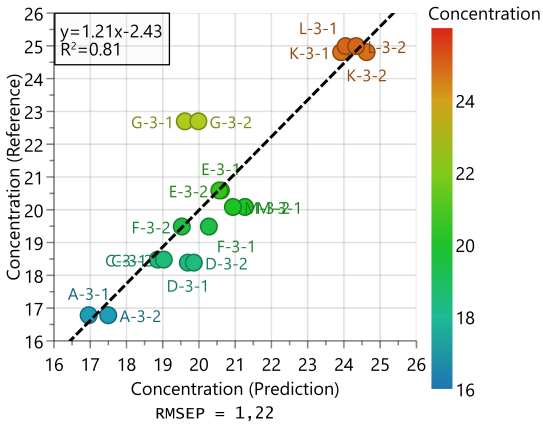

(b)

Figure 6.3: Prediction plot for API concentration a) calibration set b) test set. Tablets are labeled with three digits that represent type, replicate, and measurement number, respectively.

prediction error was around 6%. For an improved API model, the measurements should be performed in a controlled low-humidity environment, and the absorption peaks should be completely resolved by removing the water lines

and averaging the measurements.

6.3 OPLS model for tablet density

First, the spectral data were treated to reduce the noise and oscillations using the Savitzky-Golay smoothing filter. Please note that for modeling tablet density, the baseline correction was not performed because of the correlation between the baseline and tablet density through the particle size and solid fraction [65].

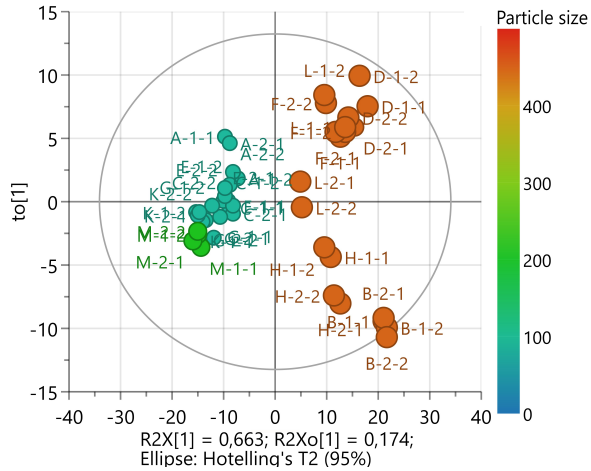

Figure 6.4: Score plot for tablet density. Tablets are clustered across the horizontal axes with respect to particle size. Tablets are labeled with three digits that represent type, replicate, and measurement number, respectively. Small and large particle sizes are shown with small and large circles, respectively.

Next, OPLS regression was applied to the calibration set, having the spectral data centered, to obtain a prediction model for the tablet density. For developing a tablet density model based on attenuation, higher frequencies were more important due to the correlation between tablet density and particle size. The OPLS score plot in Fig. 6.4 shows two clusters of training samples across the horizontal direction corresponding to the particle size. This indicates that particle size is the predictive component for tablet density. Tablets

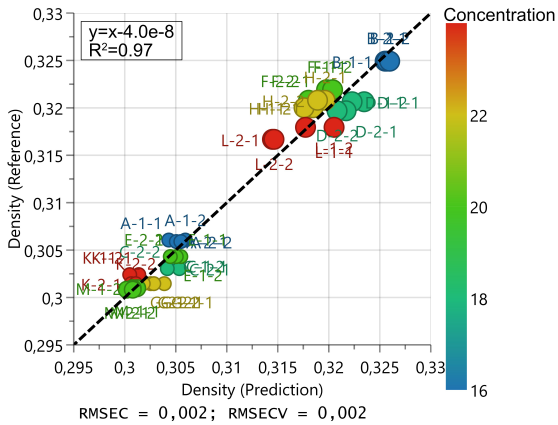

(a)

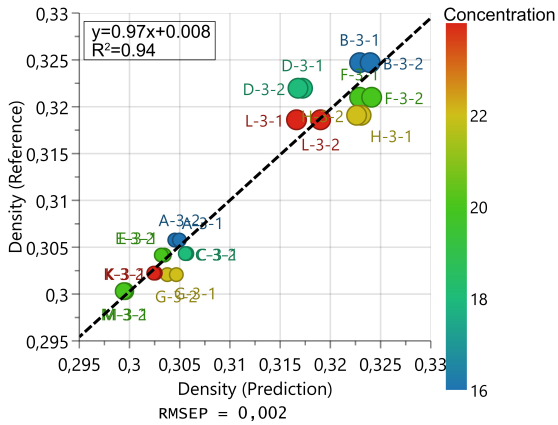

(b)

Figure 6.5: Prediction plot for tablet density a) calibration set b) test set. Tablets are labeled with three digits that represent the type, replicate, and measurement number, respectively. Small and large particle sizes are shown with small and large circles, respectively.

with larger particles are clustered on the right side marked with larger circles, and tablets with smaller particle sizes are on the left side marked with smaller

circles. The vertical direction shows the variations due to the API concentration and humidity variations. Please note that in this case, tablet series B and H were included in the tablet density model.

Fig. 6.5a shows the reference versus prediction values for tablet density. The RMSEC and RMSECV for the obtained OPLS model were both 0.002, and the R^2 was 0.97. These values show the high accuracy and the goodness of the regression model for tablet density.

Applying the test samples to the model, Fig. 6.5b presents the comparison between the reference and prediction results for the test samples. The R^2 value of 0.94, RMSEP and MBEP of 0.002 and 0.0002, together with the relative prediction error of 0.7%, show that the model is significantly accurate and precise and performs better than the OPLS model for API concentration. In both Figs. 6.5 a and b, two clusters of tablets are seen, corresponding to the particle sizes marked with smaller and larger circles, indicating that initial particle size as the main factor impacted the tablet density. Besides that, within each cluster of tablets, the API concentration increase caused the tablet density to decrease slightly, being in line with the results from our previous study [65].

CHAPTER 7

Powder flow characterisation using terahertz radar sensing

In this chapter, the characterization of powder flow properties using a terahertz radar system is presented. The results of the radar measurements show the flow properties of powder streams, like the velocity profile, back-reflected signal, and powder density distribution.

The radar beam illuminates the powder particles that pass through the beam path. The back-reflected radar signal is proportional to the powder flow density/volume concentration. Fig. 7.1 shows the side measurement results with an angle of $\theta = 5°$ on the lower part of the tube (see Fig. 4.6 c) for MCC-100 powder falling through the tube, for three consecutive radar images with a time interval of 346 ms. The radar images in Figs. 7.1(a-c) show the measured velocity of the powder particles and the intensity of the back-reflected radar signal, across the tube walls. The non-zero radar signal, together with the non-zero velocity, shows the flow of powder particles. The blue solid line indicates the measured mean velocity, $\bar{v_\theta}$.

Figs. 7.1(d-f) show the mean velocity, $\bar{v_\theta}$, and the radar signal $\sum_{v_\theta} S$, across the tube walls x_θ, where $\sum_{v_\theta} S$ is the sum of the radar signal across the velocity axis at each bin position. $\sum_{v_\theta} S$ shows a non-evenly distributed flow

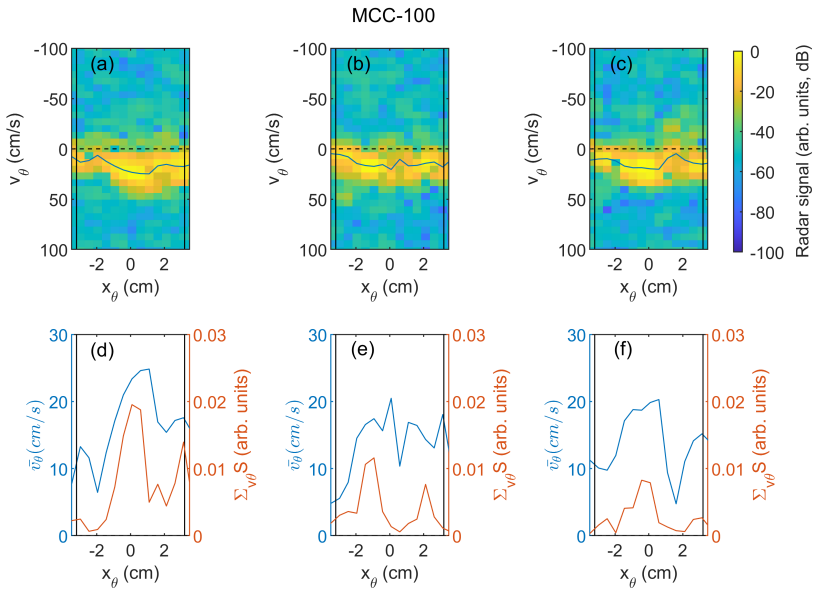

Figure 7.1: Side radar images of MCC-100 powder for three consecutive time intervals. These plots show the variation in radar signal and velocity across the tube walls and over time.

across the tube. As can be observed, besides the main core of the powder stream, other powder strings with high concentrations are also formed. This effect was also visually observed during the experiments. The change in the position of the maximum of $\sum_{v_\theta} S$ over time shows that the powder stream's core is flickering, and powder density distribution changes over time.

Vertical radar configuration gives insight into the powder falling velocity and density variations along the tube height. Fig. 7.2 shows eight consecutive radar images of falling MCC-100 powder through the tube, with a time interval of 346 m, having the radar beam incident from the bottom. The results show the velocity and radar signal distributions along the tube height, y. Figs. 7.2(a-d) show how the MCC powder flow develops with time, and Figs. 7.2(e-h) show the powder flow reaching the steady state. The solid horizontal black lines in the figures show the tube edges, while the dashed horizontal black lines mark the radar positions at the side measurements. The observed deceleration

of the powder core along the tube could be due to the powder stream flickering to the sides as traveling along the tube and consequently affecting the v_y seen by the radar. The recorded mass flow rate, $\dot{m}$, for the MCC-100 powder fall was around 1.5 g/s.

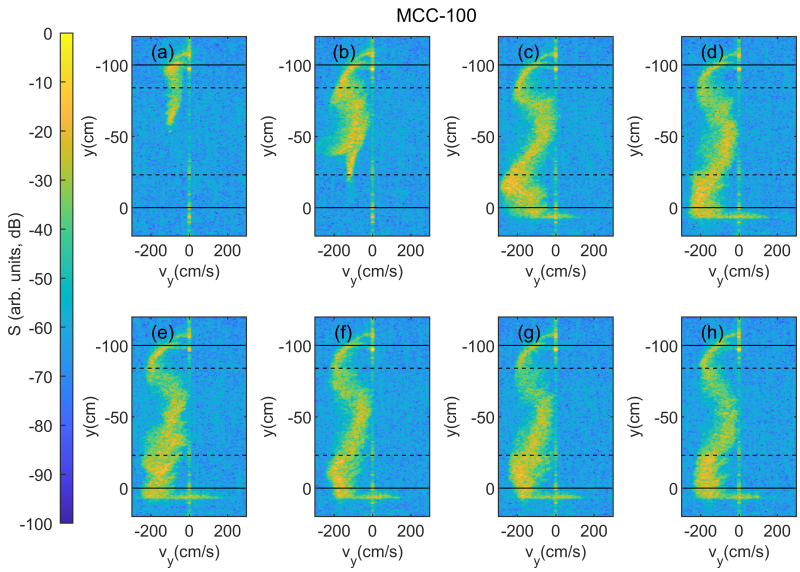

Figure 7.2: Vertical radar images of MCC-100 powder for eight consecutive time intervals. These plots show the variation in the radar signal and powder falling velocity along the tube height.

The side radar measurements have a practical interest, since this configuration can be easily implemented into the processing line, whereas the vertical realization of the radar system in industrial applications is troublesome. Therefore, in the next plots, the ability of side radar measurements to characterise different mass flow rates is explored.

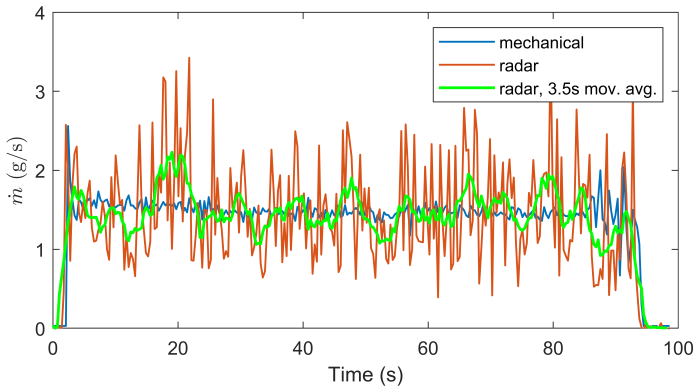

Figure 7.3: Comparison of the mass flow rate obtained with the weighing scale and total radar signal. Results of the mass flow rate obtained by the radar signal with a moving average filter over 3.5 seconds are also included.

The ability to monitor powder mass flow rate from radar side measurements is shown in Fig 7.3. This figure compares the mechanical mass flow rate obtained with the weighing scale with the one with radar side measurements configuration shown in Fig. 4.6 c, for the falling MCC-100 powder stream over time. The radar mass flow rate was obtained through the proportionality with volume concentration and powder falling velocity, see paper D. The powder flow's onset is visible in both the mechanical and radar mass flow rate. After about 90 seconds of steady-state powder flow, the powder fall decreased and stopped, captured by the mass flow rate and radar signal. It must be noticed that the radar mass flow rate fluctuations during the steady-state powder flow are much stronger than before the onset of the flow, indicating that these high amplitude fluctuations are due to real powder flow fluctuations and not noise. These fluctuations might be caused by different phenomena or a combination of them, such as Powder flickering over time, powder pulsation over time, and aggregation of powder particles. These factors change the

volume concentration/flow density, which was sensed by the radar real-time measurements, whereas not captured by the weighing scale. A moving average filter over 3.5 seconds allows the smoothing of the radar measurements to a level comparable to the mechanical mass flow rate.

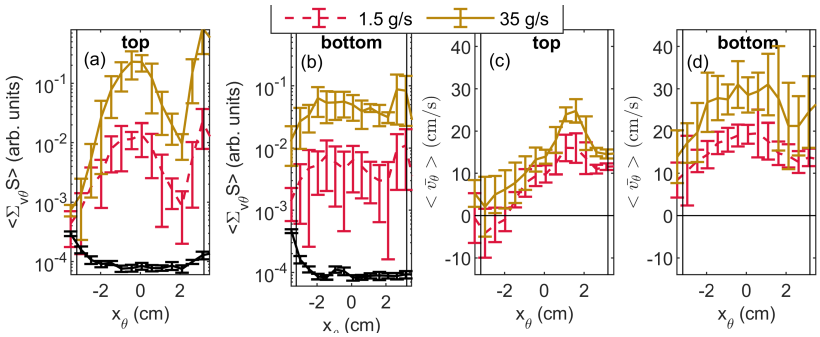

Figure 7.4: Radar signal and velocity profiles for different MCC-100 mass flow rates over ten consecutive radar images, for the radar beam incident from the side of the tube with an angle of $\theta = 5°$. Averaged radar signal, $< \sum_{v\theta} S >$, with the radar located (a) at the top position and (b) at the bottom position with respect to the tube, all for no flow, and mass flow rates of 1.5 g/s and 35 g/s of MCC-100. Averaged mean velocity, $< \bar{v_\theta} >$, with the radar located (c) on the top position and (d) on the bottom position.

In order to verify the capability of the terahertz radar in lateral configuration to characterise different flow rates inside the tube, the variation of radar signal and powder velocity for different mass flow rates for side radar measurements at the top and lower part of the tube (configurations b and c in Fig. 4.6) are shown in Fig. 7.4. Here, two extreme cases of mass flow rate were chosen for the falling MCC-100 powder particles: a low mass flow rate of $\sim$ 1.5 g/s and a high mass flow rate of $\sim$ 35 g/s. Figs. 7.4(a-d) show the average radar signal, $< \bar{S_{v\theta}} >$, and the average mean velocity, $< \bar{v_\theta} >$ over ten consecutive radar images, across the tube walls for no flow, low, and high mass flow rates. As expected, the radar signal is stronger for the higher mass flow rate at both the top and bottom radar positions due to higher powder flow density. In Fig. 7.4a, for both mass flow rates, the radar signal shows a non-uniform powder distribution across the tube walls at the top of the tube. This can be translated to a high volume concentration of particles at

the center of the tube, corresponding to the core of the powder stream, and one powder string at the vicinity of the second wall. At the bottom position, Fig. 7.4b, the radar signal shows a more uniform powder distribution across the tube, consistent with the expansion of the powder stream cross-section area when traveling down the tube. In Fig. 7.4(c-d), the powder streams with higher mass flow rates showed higher averaged mean velocity. A quantitative velocity comparison between the results from the upper and lower part of the radar is not possible due to the limited beam angle accuracy when mounting the radar.

The ability of radar side and vertical measurements for studying the flow properties of different materials and particle sizes can be found in Paper D.

CHAPTER 8

Concluding remarks and outlook

Real-time quality assessment of pharmaceutical powder blends and tablets in manufacturing processes necessitates the incorporation of fast, non-invasive, and non-destructive process analytical tools into pharmaceutical production lines. Compared to other existing techniques developed for quality assessment, THz-FD technique offers deep penetration depth, high dynamic range, lower scattering effect relative to NIR region, high spectral resolution, and a possibility for miniaturisation, and enables real-time screening of powders and tablets.

Papers A and B demonstrate the ability of THz-FDS to characterise tablet density and porosity, key physical properties of tablets that affect the disintegration and dissolution of tablets. The capability of THz-FD technique in transmission mode using a vector network analyzer (VNA) and quasi-optical components was explored to investigate the effect of the variation of materials, particle size, compaction force, and API content on tablet density and porosity. The THz-FD technique showed to be very promising in detecting the effect of small variations on tablet density and porosity, and the fragmentation behavior of the ingredients was detected by the terahertz measurements.

Paper C shows that THz-FDS combined with multivariate analysis can be

used as a complementary technique to NIR and Raman spectroscopy to quantify API content and tablet density, based on the absorption peaks and slope variations of the spectra. While NIR and Raman spectroscopy provide better prediction models for API content due to their highly selective bands with vast chemical information, THz-FDS benefits from lower scattering effects compared to the NIR region and demonstrated its suitability for the characterization of physical properties for the characterisation of tablet density.

THz-FD technique benefits from high-frequency resolution and dynamic range. The FD electronics used in papers A and B offer a high dynamic range of 100 dB in the frequency range of up to 750 GHz and a dynamic range of 60 dB for frequencies from 750 GHz to 1.5 THz, in paper C. The high dynamic range of the THz-FD technique enables the detection of minute changes in sample density and porosity.

Although, in this thesis, a bulky VNA instrument was used, in the long term, the miniaturisation capabilities of the electronic sources and detectors enable further development of a miniaturised THz-FD measurement system, which makes it promising for real-time monitoring applications.

In Paper D, the capability of a terahertz radar system to characterise powder flow in a vertical tube in real-time was investigated. The terahertz radar system offers a deep penetration depth through flowing powders with a sample volume resolution in the order of a few cubic centimeters, enabling the real-time sampling of powder flow. Moreover, the high spatial resolution of the terahertz radar, 5 mm, enables the characterization of powder flow density distribution across the pipes. Paper D shows that the radar signal was proportional to the powder flow density/volume concentration and that the stability of the powder flow can be monitored by the variations in the powder velocity profile and radar signal. The powder flow was characterized both across the tube walls, side measurements, and along the tube height, vertical measurements. The results showed that real-time mass flow rate could be obtained from radar side measurements via the back-reflected radar signal and the measured velocity. This could be of great interest in industrial applications since powder flow distribution, density, and mass flow rate are critical parameters in pharmaceutical operations.

The powder flows investigated in this thesis consisted of one single pharmaceutical ingredient. In future work, the characterization of powder flow consisting of a blend of several ingredients should be studied, addressing the

challenge of differentiating variations in flow density from variations in blend concentration. Advanced machine learning techniques or the use of two radar systems with different operating frequencies can be a possible solution to tackle this challenge.

As a step towards industrialization, terahertz radar sensing for powder flows in metallic tubes should be tested, since the manufacturing vessels are typically made of stainless steel. This would be feasible by providing a terahertz transparent window in metallic pipes and tilting the radar system with a small angle to minimize the strong back reflection from the second wall of the tube.

In conclusion, the THz-FD technique and terahertz FMCW radar show great potential to be utilized as a process analytical tool for in-process monitoring of powders and tablets in pharmaceutical applications, in batch and especially in continuous processes. On top of that, this technique could be implemented in other industries, for example the food industry, seeking real-time monitoring solutions for the quality assurance of continuous processes, ensuring sustainability by efficiency in productivity, production costs, and time.

CHAPTER 9

Summary of appended papers

Paper A

Non-Destructive Characterization of Pharmaceutical Tablets Using Terahertz Frequency Domain Spectroscopy

In this paper, terahertz frequency domain spectroscopy (THz-FDS) in transmission mode is used to extract the effective permittivity of tablets at 325-500 GHz. The sensitivity of terahertz waves to the change of dielectric constant and the correlation between effective permittivity and tablet density were studied. The samples under study included Microcrystalline cellulose (MCC), Benzophenone, and Succinic acid. In each set, various compaction forces were applied during the tablet compression to produce tablets with different tablet densities. The results showed that terahertz waves were sensitive to the change of materials and compaction force. Moreover, a linear correlation between effective permittivity and tablet density was observed.
My contribution: I designed the experiments, performed the measurements, analysed the data, and with the feedback from my co-authors, wrote the paper.

Paper B

Terahertz Frequency Domain Sensing for Fast Porosity Measurement of Pharmaceutical Tablets

In this paper, the THz-FD technique was explored as a fast, non-destructive, and sensitive technique for the porosity measurement of pharmaceutical tablets. A sample set of 69 tablets with the design factors, such as particle size, API concentration, and compaction force, was studied. The samples were measured in transmission mode across the frequency range 500-750 GHz, using a vector network analyzer combined with a quasi-optical set-up to guide and focus the beam. The effective refractive index of tablets was obtained from complex transmission coefficients and then was translated to porosity, using an empirical linear model. The results show that the THz-FD technique was highly sensitive to the variations of the design factors, showing that filler particle size and compaction force had a significant impact on porosity. Moreover, a fragmentation behavior of particles was observed by THz porosity measurements and was verified with scanning electron microscopy of the cross-section of tablets.
My contribution: I designed the experiments, performed the measurements, analysed the data, and with the feedback from my co-authors, wrote the paper.

Paper C

Terahertz frequency-domain sensing combined with quantitative multivariate analysis for pharmaceutical tablet inspection

The applicability of THz-FDS combined with multivariate analysis was explored to quantify API concentration and tablet density based on the attenuation spectral data from 750 GHz to 1.5 THz. The tablets were divided into training and test sets, and orthogonal partial least square regression was applied to training samples and later to test samples to develop and assess the prediction models. The API model was obtained based on the changes in absorption peak characteristics of the API and excipient, whereas the tablet density model was obtained based on the slope variations of the spectra as a

result of variation in particle size. The variation of API had an insignificant effect on the tablet density. The results showed that a fair model with a relative prediction error of 6 % was obtained for the API content, and an excellent model with a relative prediction error of less than 1 % for tablet density.
My contribution: I designed the experiments, performed the measurements, analysed the data, and with the feedback from my co-authors, wrote the paper.

Paper D

Terahertz radar diagnostics of powder dynamics in pharmaceutical manufacturing

The applicability of terahertz radar sensing for the real-time characterization of pharmaceutical powders was explored. An experimental setup for flowing the powder particles with different mass flow rates, materials, and particle sizes was designed. Terahertz radar measurements at a center frequency of 340 GHz were successfully performed to study the velocity profile and flow density distribution/variation of powder particles across and along the tube. The back-reflected radar signal was proportional to the powder density. The velocity profile, together with the radar signal, presented the stability information of the powder stream over time.
My contribution: I designed the experiments, performed the measurements, post-processing and data analysis together with M. Bonman, and with the feedback from my co-authors, wrote the paper.

References

[1] "An Introduction to Powders Author – Tim Freeman , Managing Director , Freeman Technology Introduction,"

[2] T. Ervasti, P. Silfsten, J. Ketolainen, and K. E. Peiponen, "A study on the resolution of a terahertz spectrometer for the assessment of the porosity of pharmaceutical tablets," *Applied Spectroscopy*, vol. 66, no. 3, pp. 319–323, 2012. DOI: 10.1366/11-06315.

[3] P. Bawuah, N. Tan, S. N. A. Tweneboah, *et al.*, "Terahertz study on porosity and mass fraction of active pharmaceutical ingredient of pharmaceutical tablets," *European Journal of Pharmaceutics and Biopharmaceutics*, vol. 105, pp. 122–133, 2016. DOI: 10.1016/j.ejpb.2016.06.007.

[4] O. Berntsson, L. G. Danielsson, B. Lagerholm, and S. Folestad, "Quantitative in-line monitoring of powder blending by near infrared reflection spectroscopy," *Powder Technology*, vol. 123, no. 2-3, 2002, ISSN: 00325910. DOI: 10.1016/S0032-5910(01)00456-9.

[5] R. Gosselin, P. Durão, N. Abatzoglou, and J. M. Guay, "Monitoring the concentration of flowing pharmaceutical powders in a tableting feed frame," *Pharmaceutical Development and Technology*, vol. 22, no. 6, 2017, ISSN: 10979867. DOI: 10.3109/10837450.2015.1102278.

[6] F. De Leersnyder, E. Peeters, H. Djalabi, *et al.*, "Development and validation of an in-line NIR spectroscopic method for continuous blend potency determination in the feed frame of a tablet press," *Journal of*

Pharmaceutical and Biomedical Analysis, vol. 151, 2018, ISSN: 1873264X. DOI: 10.1016/j.jpba.2018.01.032.

[7] R. C. Lyon, D. S. Lester, E. N. Lewis, *et al.*, "Near-infrared spectral imaging for quality assurance of pharmaceutical products: Analysis of tablets to assess powder blend homogeneity," *AAPS PharmSciTech*, vol. 3, no. 3, 2002, ISSN: 15309932. DOI: 10.1007/BF02830615.

[8] M. Khorasani, J. M. Amigo, C. C. Sun, P. Bertelsen, and J. Rantanen, "Near-infrared chemical imaging (NIR-CI) as a process monitoring solution for a production line of roll compaction and tableting," *European Journal of Pharmaceutics and Biopharmaceutics*, vol. 93, 2015, ISSN: 18733441. DOI: 10.1016/j.ejpb.2015.04.008.

[9] I. Jedvert, M. Josefson, and F. Langkilde, "Quantification of an active substance in a tablet by NIR and Raman spectroscopy," *Journal of Near Infrared Spectroscopy*, vol. 6, no. 1-4, 1998, ISSN: 09670335. DOI: 10.1255/jnirs.148.

[10] G. J. Vergote, T. R. De Beer, C. Vervaet, *et al.*, "In-line monitoring of a pharmaceutical blending process using FT-Raman spectroscopy," *European Journal of Pharmaceutical Sciences*, vol. 21, no. 4, 2004, ISSN: 09280987. DOI: 10.1016/j.ejps.2003.11.005.

[11] M. G. Rasteiro, R. Silva, F. A. Garcia, and P. Faia, *Electrical tomography: A review of configurations and applications to particulate processes*, 2011. DOI: 10.14356/kona.2011010.

[12] C. E. Davies, S. J. Tallon, and N. Brown, "Continuous monitoring of bulk density and particle size in flowable powders and grains," *Chemical Engineering Research and Design*, vol. 83, no. 7 A, 2005, ISSN: 02638762. DOI: 10.1205/cherd.04325.

[13] S. Stranzinger, D. Markl, J. G. Khinast, and A. Paudel, "Review of sensing technologies for measuring powder density variations during pharmaceutical solid dosage form manufacturing," *TrAC - Trends in Analytical Chemistry*, vol. 135, p. 116 147, 2021, ISSN: 18793142. DOI: 10.1016/j.trac.2020.116147.

[14] P. H. Siegel, "Terahertz technology," *IEEE Transactions on Microwave Theory and Techniques*, vol. 50, no. 3, pp. 910–928, 2002, ISSN: 00189480. DOI: 10.1109/22.989974.

[15] M. Claybourn, H. Yang, L. Gradinarsky, J. Johansson, and S. Folestad, "Terahertz Spectroscopy for Pharmaceutical Applications," in *Handbook of Vibrational Spectroscopy*, 2007. DOI: 10.1002/9780470027325.s8914.

[16] X. Lu, H. Sun, T. Chang, J. Zhang, and H. L. Cui, "Terahertz detection of porosity and porous microstructure in pharmaceutical tablets: A review," *International Journal of Pharmaceutics*, vol. 591, no. October, p. 120 006, 2020. DOI: 10.1016/j.ijpharm.2020.120006.

[17] M. Juuti, H. Tuononen, T. Prykäri, *et al.*, "Optical and terahertz measurement techniques for flat-faced pharmaceutical tablets: A case study of gloss, surface roughness and bulk properties of starch acetate tablets," *Measurement Science and Technology*, vol. 20, no. 1, 2009. DOI: 10.1088/0957-0233/20/1/015301.

[18] P. Bawuah, A. Pierotic Mendia, P. Silfsten, *et al.*, "Detection of porosity of pharmaceutical compacts by terahertz radiation transmission and light reflection measurement techniques," *International Journal of Pharmaceutics*, vol. 465, no. 1-2, pp. 70–76, 2014. DOI: 10.1016/j.ijpharm.2014.02.011.

[19] M. Naftaly, I. Tikhomirov, P. Hou, and D. Markl, "Measuring open porosity of porous materials using thz-tds and an index-matching medium," *Sensors (Switzerland)*, vol. 20, no. 11, 2020. DOI: 10.3390/s20113120.

[20] A. L. Skelbæk-Pedersen, M. Anuschek, T. K. Vilhelmsen, J. Rantanen, and J. A. Zeitler, "Non-destructive quantification of fragmentation within tablets after compression from scattering analysis of terahertz transmission measurements," *International Journal of Pharmaceutics*, vol. 588, Oct. 2020. DOI: 10.1016/j.ijpharm.2020.119769.

[21] S. Stranzinger, E. Faulhammer, J. Li, *et al.*, "Measuring bulk density variations in a moving powder bed via terahertz in-line sensing," *Powder Technology*, vol. 344, pp. 152–160, 2019. DOI: 10.1016/j.powtec.2018.11.106.

[22] P. F. Neumaier, H. Richter, J. Stake, *et al.*, "Molecular spectroscopy with a compact 557-GHz heterodyne receiver," *IEEE Transactions on Terahertz Science and Technology*, vol. 4, no. 4, 2014. DOI: 10.1109/TTHZ.2014.2326554.

[23] R. Dahlbäck, T. Rubaek, M. Persson, and J. Stake, "A system for THz imaging of low-contrast targets using the born approximation," *IEEE Transactions on Terahertz Science and Technology*, vol. 2, no. 3, 2012. DOI: 10.1109/TTHZ.2012.2189900.

[24] K. Sengupta, T. Nagatsuma, and D. M. Mittleman, "Terahertz integrated electronic and hybrid electronic–photonic systems," *Nature Electronics*, vol. 1, no. 12, 2018. DOI: 10.1038/s41928-018-0173-2.

[25] P. Hillger, J. Grzyb, R. Jain, and U. R. Pfeiffer, "Terahertz Imaging and Sensing Applications With Silicon-Based Technologies," *IEEE Transactions on Terahertz Science and Technology*, vol. 9, no. 1, 2019. DOI: 10.1109/TTHZ.2018.2884852.

[26] T. Bryllert, M. Bonmann, and J. Stake, "A Submillimeter-Wave FMCW Pulse-Doppler Radar to Characterize the Dynamics of Particle Clouds," *IEEE Transactions on Terahertz Science and Technology*, vol. 13, no. X, pp. 1–7, 2023. DOI: DOI:10.1109/TTHZ.2023.3263641.

[27] P. Bawuah and J. A. Zeitler, *Advances in terahertz time-domain spectroscopy of pharmaceutical solids: A review*, Jun. 2021. DOI: 10.1016/j.trac.2021.116272.

[28] J.-L. Coutaz, F. Garet, and V. P. Wallace, *Principles of Terahertz Time-Domain Spectroscopy*. 2018. DOI: 10.1201/b22478.

[29] J. L. Hesler, Y. Duan, B. Foley, and T. W. Crowe, "THz vector network analyzer measurements and calibration," in *21st International Symposium on Space Terahertz Technology 2010, ISSTT 2010*, 2010.

[30] D. K. George, A. Charkhesht, and N. Q. Vinh, "New terahertz dielectric spectroscopy for the study of aqueous solutions," *Review of Scientific Instruments*, vol. 86, no. 12, 2015, ISSN: 10897623. DOI: 10.1063/1.4936986.

[31] D. Pozar, *Microwave Engineering Fourth Edition*. 2005. DOI: TK7876.P692011.

[32] R. Marks and D. Williams, "A general waveguide circuit theory," *Journal of Research of the National Institute of Standards and Technology*, vol. 97, no. 5, 1992, ISSN: 1044-677X. DOI: 10.6028/jres.097.024.

[33] C. B. S, "Conversions Between S, 2, Y, h, ABCD, and T Parameters which are Valid for Complex Source and Load Impedances," *IEEE Transactions on Microwave Theory and Techniques*, vol. 42, no. 2, pp. 205–211, 1994. DOI: doi:10.1109/22.275248.

[34] C. F. Bohren, *Absorption and scattering of light by small particles*. 1983. DOI: 10.1088/0031-9112/35/3/025.

[35] "Radio detection and ranging," *Nature*, vol. 152, no. 3857, 1943, ISSN: 00280836. DOI: 10.1038/152391b0.

[36] M. I. Skolnik, *Introduction to radar systems / M.I. Skolnik*. 2001.

[37] K. B. Cooper, "Submillimeter-Wave Radar: Solid-State System Design and Applications," no. November, pp. 51–67, 2014.

[38] G. Thoorens, F. Krier, B. Leclercq, B. Carlin, and B. Evrard, *Microcrystalline cellulose, a direct compression binder in a quality by design environment - A review*, 2014. DOI: 10.1016/j.ijpharm.2014.06.055.

[39] J. Merrylin, R. Y. Kannah, J. R. Banu, and I. T. Yeom, "Production of organic acids and enzymes/biocatalysts from food waste," in *Food Waste to Valuable Resources*, 2020. DOI: 10.1016/b978-0-12-818353-3.00006-7.

[40] IARC, "IARC Monograph. Some chemicals present in industrial and consumer products, food and drinking-water.," in *IARC Scientific Publications*, 2012.

[41] K. D. Rainsford, *Ibuprofen: Pharmacology, efficacy and safety*, 2009. DOI: 10.1007/s10787-009-0016-x.

[42] L. X. Liu, I. Marziano, A. C. Bentham, J. D. Litster, E.T.White, and T. Howes, "Effect of particle properties on the flowability of ibuprofen powders," *International Journal of Pharmaceutics*, vol. 362, no. 1-2, pp. 109–117, 2008. DOI: 10.1016/j.ijpharm.2008.06.023.

[43] A. S. Narang and S. I. Badawy, *Handbook of pharmaceutical wet granulation: Theory and practice in a quality by design paradigm*. 2018. DOI: 10.1016/C2016-0-00287-5.

[44] G. Morin and L. Briens, "The effect of lubricants on powder flowability for pharmaceutical application," *AAPS PharmSciTech*, vol. 14, no. 3, 2013, ISSN: 15309932. DOI: 10.1208/s12249-013-0007-5.

[45] D. Bourreau, A. Péden, and S. Le Maguer, "A quasi-optical free-space measurement setup without time-domain gating for material characterization in the W-band," *IEEE Transactions on Instrumentation and Measurement*, vol. 55, no. 6, pp. 2022–2028, 2006. DOI: 10.1109/TIM.2006.884283.

[46] A. M. Nicolson and G. F. Ross, "Measurement of the Intrinsic Properties Of Materials by Time-Domain Techniques," *IEEE Transactions on Instrumentation and Measurement*, vol. 19, no. 4, pp. 377–382, 1970. DOI: 10.1109/TIM.1970.4313932.

[47] W. B. Weir, "Automatic Measurement of Complex Dielectric Constant and Permeability at Microwave Frequencies," *Proceedings of the IEEE*, vol. 62, no. 1, pp. 33–36, 1974. DOI: 10.1109/PROC.1974.9382.

[48] M. Mrnka, R. Appleby, and E. Saenz, "Accurate S-parameter Modeling and Material Characterization in Quasi-Optical Systems," *IEEE Transactions on Terahertz Science and Technology*, no. c, pp. 1–1, 2022. DOI: 10.1109/tthz.2021.3140201.

[49] S. Trabelsi, A. W. Kraszewski, and S. O. Nelson, "Phase-shift ambiguity in microwave dielectric properties measurements," *IEEE Transactions on Instrumentation and Measurement*, vol. 49, no. 1, 2000, ISSN: 00189456. DOI: 10.1109/19.836309.

[50] C. Sun, "A Novel Method for Deriving True Density of Pharmaceutical Solids Including Hydrates and Water-Containing Powders," *Journal of Pharmaceutical Sciences*, vol. 93, no. 3, pp. 646–653, 2004. DOI: 10.1002/jps.10595.

[51] A. Moradi, M. Lindsjo, J. Stake, S. Folestad, and H. Rodilla, "Non-Destructive Characterization of Pharmaceutical Tablets Using Terahertz Frequency Domain Spectroscopy," *International Conference on Infrared, Millimeter, and Terahertz Waves, IRMMW-THz*, vol. 2019-Septe, pp. 3–4, 2019. DOI: 10.1109/IRMMW-THz.2019.8874004.

[52] R. Bro, "Multivariate calibration: What is in chemometrics for the analytical chemist?" In *Analytica Chimica Acta*, vol. 500, 2003. DOI: 10.1016/S0003-2670(03)00681-0.

[53] J. Trygg and S. Wold, "Orthogonal projections to latent structures (O-PLS)," *Journal of Chemometrics*, vol. 16, no. 3, 2002, ISSN: 08869383. DOI: 10.1002/cem.695.

[54] T. Bryllert, M. Bonmann, and J. Stake, "340 GHz FMCW pulse-Doppler radar to characterize the dynamics of particle clouds," vol. 13, no. X, pp. 1–7, 2023.

[55] Douglas C. Montgomery, *Montgomery: Design and Analysis of Experiments*, 2000.

[56] Sartorius Stedim Data Analytics, *User Guide to MODDE - Version 12*, 2017.

[57] G. Alderborn and C. Nyström, "Studies on direct compression of tablets XIV. The effect of powder fineness on the relation between tablet permeametry surface area and compaction pressure," *Powder Technology*, vol. 44, no. 1, pp. 37–42, 1985. DOI: 10.1016/0032-5910(85)85018-X.

[58] A. Moradikouchi, A. Sparen, S. Folestad, J. Stake, and H. Rodilla, "Small Variation of Active Pharmaceutical Ingredient Concentration Can Be Observed with THz Frequency Domain Spectroscopy," *2021 46th International Conference on Infrared, Millimeter and Terahertz Waves, IRMMW-THz*, pp. 1–1, 2021. DOI: 10.1109/irmmw-thz50926.2021.9567162.

[59] N. Tarlier, I. Soulairol, N. Sanchez-Ballester, *et al.*, "Deformation behavior of crystallized mannitol during compression using a rotary tablet press simulator," *International Journal of Pharmaceutics*, vol. 547, no. 1-2, pp. 142–149, 2018. DOI: 10.1016/j.ijpharm.2018.05.026.

[60] V. N. Le, P. Leterme, A. Gayot, and M. P. Flament, "Influence of granulation and compaction on the particle size of ibuprofen-Development of a size analysis method," *International Journal of Pharmaceutics*, vol. 321, no. 1-2, pp. 72–77, 2006. DOI: 10.1016/j.ijpharm.2006.05.010.

[61] A. Sparén, M. Hartman, M. Fransson, J. Johansson, and O. Svensson, "Matrix effects in quantitative assessment of pharmaceutical tablets using transmission raman and near-infrared (NIR) Spectroscopy," *Applied Spectroscopy*, vol. 69, no. 5, pp. 580–589, 2015, ISSN: 0. DOI: 10.1366/14-07645.

[62] W. Chen, Y. Peng, X. Jiang, J. Zhao, H. Zhao, and Y. Zhu, "Isomers Identification of 2-hydroxyglutarate acid disodium salt (2HG) by Terahertz Time-domain Spectroscopy," *Scientific Reports*, vol. 7, no. 1, 2017, ISSN: 20452322. DOI: 10.1038/s41598-017-11527-z.

[63] A. Savitzky and M. J. Golay, "Smoothing and Differentiation of Data by Simplified Least Squares Procedures," *Analytical Chemistry*, vol. 36, no. 8, 1964, ISSN: 15206882. DOI: 10.1021/ac60214a047.

[64] J. Peng, S. Peng, A. Jiang, J. Wei, C. Li, and J. Tan, "Asymmetric least squares for multiple spectra baseline correction," *Analytica Chimica Acta*, vol. 683, no. 1, 2010, ISSN: 00032670. DOI: 10.1016/j.aca.2010.08.033.

[65] A. Moradikouchi, A. Sparén, S. Folestad, J. Stake, and H. Rodilla, "Terahertz frequency domain sensing for fast porosity measurement of pharmaceutical tablets," *International Journal of Pharmaceutics*, vol. 618, 2022, ISSN: 18733476. DOI: 10.1016/j.ijpharm.2022.121579.